JGR Oceans

RESEARCH ARTICLE
10.1029/2024JC022126

Open Ocean Versus Upwelling Regimes: Air-Sea CO_2 Fluxes and pCO_2 Inter-Annual Variability in the Southern California Current System

Helena C. Frazão[1], Uwe Send[1], Adrienne J. Sutton[2], Mark D. Ohman[1], Matthias Lankhorst[1], Todd R. Martz[1], and Jeffrey Sevadjian[1]

[1]Scripps Institution of Oceanography, University of California San Diego, La Jolla, CA, USA, [2]Pacific Marine Environmental Laboratory, National Oceanic and Atmospheric Administration (PMEL/NOAA), Seattle, WA, USA

Abstract Two moorings equipped with autonomous air-sea CO_2 instrumentation located in the Southern California Current System were used to examine the seasonal and interannual variability of the surface partial pressure of carbon dioxide in seawater ($pCO_{2,sw}$) and the air-sea CO_2 flux between 2008 and 2022. These two moorings are in two distinct oceanographic regimes: offshore, centered in the California Current (CCE1), and nearshore within the coastal upwelling regime (CCE2). The offshore seasonal cycles of the surface $pCO_{2,sw}$ and CO_2 flux are driven by sea surface temperature (SST) seasonality and at the nearshore site by dissolved inorganic carbon (DIC) concentration changes linked with seasonal upwelling. The resulting net annual CO_2 flux at CCE1 is -0.52 molC m^{-2} $year^{-1}$ (sink), while at CCE2, the best estimate for the long-term CO_2 flux mean is 0.23 molC m^{-2} $year^{-1}$ (source). The interannual variability at the offshore site is mainly controlled by SST, where warm anomalies (El Niño and Marine Heatwaves) cause anomalous CO_2 outgassing, and cold anomalies (La Niña) increase CO_2 ingassing. Conversely, at the nearshore site, the strength (or absence of) upwelling of DIC-rich water associated with cold (or warm anomalies) results in increased outgassing (or ingassing) of CO_2. Long-term trends in $pCO_{2,sw}$ approximately follow the atmospheric CO_2 increase. At the offshore site, the DIC trend is consistent with air-sea fluxes, keeping the CO_2 equilibrium between air and water. At the nearshore site, the DIC trend has a similar magnitude but could also result from changing water-mass composition or concentration due to freshwater loss.

Plain Language Summary The ocean is a good reservoir for the atmosphere's excess carbon dioxide (CO_2). It absorbs CO_2 when the concentration in water is lower than the atmosphere and outgasses CO_2 when the concentration in water is higher than the atmosphere. When the seawater temperature increases, the ocean CO_2 increases; therefore, temperature changes affect CO_2 exchange between ocean and atmosphere. However, other factors influence the amount of CO_2 the ocean absorbs. To identify the relevant processes, we placed two stations in the Southern California Current measuring CO_2 in the air and seawater since 2008—CCE1 is in the open ocean while CCE2 is closer to the coast. These measurements show how seawater CO_2 changes on multiple timescales. In the open-ocean area, the seawater CO_2 is driven by surface temperature, whereas closer to the coast, it is affected by vertical movement of water during spring, which injects CO_2-rich water into the surface. Annually, the open-ocean station absorbs CO_2 while the nearshore station releases CO_2 on average. Furthermore, we observe that warm anomalies, such as marine heatwaves or El Niño, change the average behavior of these two stations: the ocean releases CO_2 into the atmosphere offshore but absorbs CO_2 closer to the coast.

Key Points:

- The open ocean site is a net annual CO_2 sink while the seasonal upwelling site is a net annual CO_2 source
- At the offshore site, warm anomalies, such as El Niño and Marine heatwaves, result in CO_2 outgassing driven by sea surface temperature
- Nearshore, warm anomalies result in CO_2 uptake, explained by the absence of upwelling, outweighing the competing temperature effect

Supporting Information:

Supporting Information may be found in the online version of this article.

Correspondence to:

H. C. Frazão,
hvieirafrazao@ucsd.edu

Citation:

Frazão, H. C., Send, U., Sutton, A. J., Ohman, M. D., Lankhorst, M., Martz, T. R., & Sevadjian, J. (2025). Open ocean versus upwelling regimes: Air-sea CO_2 fluxes and pCO_2 inter-annual variability in the Southern California Current System. *Journal of Geophysical Research: Oceans*, *130*, e2024JC022126. https://doi.org/10.1029/2024JC022126

Received 13 NOV 2024
Accepted 16 MAY 2025

Author Contributions:

Conceptualization: Helena C. Frazão
Formal analysis: Helena C. Frazão, Matthias Lankhorst, Todd R. Martz
Funding acquisition: Uwe Send, Mark D. Ohman
Investigation: Uwe Send, Adrienne J. Sutton, Mark D. Ohman
Methodology: Helena C. Frazão
Supervision: Uwe Send
Validation: Adrienne J. Sutton, Matthias Lankhorst, Jeffrey Sevadjian
Visualization: Helena C. Frazão
Writing – original draft: Helena C. Frazão

1. Introduction

The capacity of the ocean to absorb carbon dioxide (CO_2) renders it a crucial reservoir for anthropogenic CO_2, playing an important role in climate regulation. The global ocean has absorbed approximately 25% of anthropogenic CO_2 emissions since the industrial era (Gruber et al., 2023; Le Quéré et al., 2016; Sabine et al., 2004). However, many global ocean CO_2 uptake estimations often do not fully account for the contribution from the nearshore margin (Gruber, 2015). Recent estimates suggest that coastal margins contributed 7%–17% to global CO_2 uptake (Cai, 2011; Gruber, 2015; Laruelle et al., 2010, 2014). Understanding the spatiotemporal variability of CO_2 uptake on multiple scales and its underlying driving processes is essential to assess the carbon cycle and ocean acidification.

Writing – review & editing: Helena C. Frazão, Uwe Send, Adrienne J. Sutton, Mark D. Ohman, Matthias Lankhorst, Todd R. Martz, Jeffrey Sevadjian

The North Pacific basin between 30°N and 40°–45°N is an important net annual sink for atmospheric CO_2, contributing to 20%–25% of the global ocean CO_2 uptake (Ishii et al., 2014; Takahashi et al., 2002, 2009). The air-sea CO_2 fluxes in this region follow a seasonal pattern linked with variations in the difference of the partial pressure of pCO_2 (ΔpCO_2) between surface waters ($pCO_{2,sw}$) and near-surface atmosphere ($pCO_{2,air}$). Seasonal ΔpCO_2 variability mainly drives changes in air-sea CO_2 fluxes, which is influenced by a series of physical and biological processes (Chen et al., 2021; Palevsky & Quay, 2017; Sutton et al., 2017; Xiu & Chai, 2014). The subtropical to mid-latitudes in the North Pacific Ocean have been found to behave as a CO_2 sink during the cold season and as a CO_2 source during the warm season (Chen & Hu, 2019; Landschützer et al., 2016; Takahashi et al., 2002; Turi et al., 2014). While the annual cycle and trends of $pCO_{2,air}$ are well understood in the North Pacific, $pCO_{2,sw}$ annual cycle and trends primarily rely on limited shipboard underway observations and sparse moored buoys (e.g., Sutton et al., 2017, 2019). Therefore, in most locations, $pCO_{2,sw}$ variability remains poorly constrained at sub-seasonal scales. To address this, various methods (e.g., Chen et al., 2016; Friedlingstein et al., 2023; Landschützer et al., 2019 and references therein) have been employed to generate new regional and global $pCO_{2,sw}$ products (e.g., Fay et al., 2021; Gregor & Gruber, 2021; Laruelle et al., 2017; Sharp et al., 2022). When combined with in situ measurements, these methods have improved our understanding of the processes controlling $pCO_{2,sw}$. These include biological processes driving carbon export into the deep ocean (Palevsky & Quay, 2017), water mass advection, and ocean circulation (Ayers & Lozier, 2012). However, many of these studies do not include coastal regimes due to the limited number of observations combined with the highly dynamic physical and biogeochemical environment.

The California Current System (CCS) in the Northeast Pacific is one of the best observed Eastern Boundary Upwelling Systems worldwide. It is characterized by strong seasonal upwelling that intensifies in spring, bringing waters rich in macronutrients and trace metals to the near-surface. These waters fuel primary production and contribute to the region's fisheries' productivity. Although upwelled waters exhibit high dissolved inorganic carbon (DIC) content that can potentially increase $pCO_{2,sw}$ levels above those in the near-surface atmosphere (e.g., Friederich et al., 2002; Hales et al., 2012; Sharp et al., 2022), thereby promoting CO_2 outgassing, a variety of processes in surface waters rapidly restore the equilibrium state, as noted by Turi et al. (2014). Beyond the California Current transitional zone (>100 km from shore; Kosro et al., 1991), the CCS behaves similarly to the North Pacific gyre, with higher $pCO_{2,sw}$ during summer and lower values during winter, in phase with sea surface temperature (SST) variations (Chen & Hu, 2019; Takahashi et al., 2002; Turi et al., 2014). Closer to shore, estimating CO_2 uptake in the CCS has been challenging due to the complex nearshore spatiotemporal variability in $pCO_{2,sw}$ and air-sea CO_2 fluxes. Cai et al. (2006) and Sharp et al. (2022) observed net outgassing along the southern CCS shelf but net carbon uptake in the northern part. Nevertheless, the CCS region is estimated to be a net CO_2 sink (Fiechter et al., 2014; Hales et al., 2012; Turi et al., 2014).

In the CCS, El Niño Southern Oscillation (ENSO) is the dominant mode of interannual variability, and its effects are pronounced (e.g., Capotondi et al., 2015; McClatchie et al., 2016; Thompson et al., 2022). Gruber et al. (2023) reported that the Pacific is the only basin where a clear interannual signal can be observed superimposed on the long-term trend of air-sea CO_2 flux. Warm anomalies associated with El Niño suppress upwelling along the California coast (Jacox et al., 2015), reducing nutrient and carbon fluxes from subsurface waters to the surface. This contributes to reducing $pCO_{2,sw,}$ and thus air-sea CO_2 exchange (Friederich et al., 2002). Conversely, upwelling events intensify during La Niña, leading to high $pCO_{2,sw,}$ and outgassing of CO_2.

In addition to ENSO, the CCS is influenced by other climate patterns, including the Pacific Decadal Oscillation (PDO; Zhang et al., 1997) and the North Pacific Gyre Oscillation (NPGO; Di Lorenzo et al., 2008; Chenillat et al., 2012; Crawford et al., 2018). These modes of variability impact biogeochemistry and the ocean's CO_2 uptake capacity by inducing changes in mixing, ocean currents, and water properties. Marine heatwaves (MHW) also impact CCS but are often unrelated to ENSO (Dalsin et al., 2023; Fumo et al., 2020; Wei et al., 2021), and their frequency in the CCS has increased over the past decade (Fumo et al., 2020). Although MHWs' role in air-sea CO_2 flux in the CCS has not received much attention, they significantly decrease CO_2 uptake in the North Pacific (Mignot et al., 2022). The authors state that MHWs' impact on CO_2 fluxes results from two competing mechanisms: (a) decreased CO_2 solubility due to rising SST and (b) increased water column stratification, thus reducing vertical mixing with underlying rich-CO_2 waters. One of the most significant MHWs in the Northeast Pacific occurred in 2014/2015, known as the North Pacific Warm Anomaly or Blob 1.0. This MHW reduced surface $pCO_{2,sw,}$ and DIC concentration in the North Pacific due to reduced mixing and atypical advection (Franco et al., 2021; Kohlman et al., 2024; Mogen et al., 2022), which is expected to enhance air-sea CO_2 flux

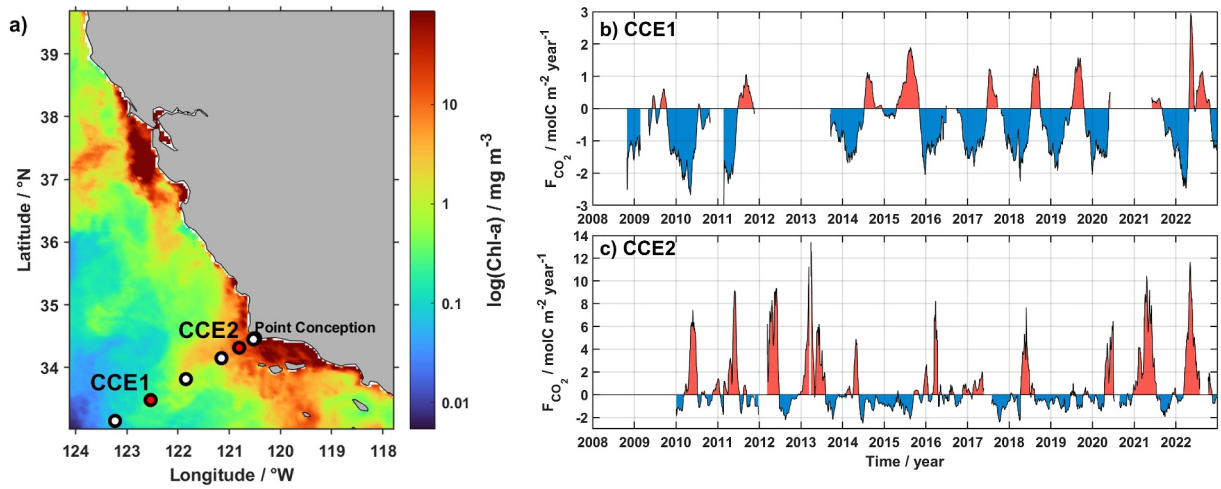

Figure 1. (a) Location of the CCE moorings in the Southern California Current System. White and red dots are stations along CalCOFI line 80. Red dots show the positions of the CCE1 and CCE2 moorings. Plotted as background is a month-long composite of logarithmic Chlorophyll *a* (Chl-a) concentration during the strong La Niña in May 2022, acquired by the MODIS Aqua satellite (data available at https://oceancolor.gsfc.nasa.gov/l3/). (b) Air-sea surface CO_2 fluxes at CCE1 and (c) CCE2 mooring sites. Red-shaded periods indicate CO_2 outgassing into the atmosphere (positive fluxes), and blue represents periods of CO_2 uptake by the ocean (negative fluxes). The CO_2 flux time series are smoothed with a 30-day running mean filter. Note that the *y*-axis scales differ for the two moorings.

(Duke et al., 2023). However, the role of MHWs in the nearshore air-sea CO_2 flux in the CCS remains to be understood. High-frequency and extended observations of coastal and open-ocean $pCO_{2,sw}$, and environmental conditions are useful to address the variability across multiple temporal scales.

In this study, we analyze sustained pCO_2 measurements from two moorings in the Southern California Current System (SCCS) along CalCOFI line 80 (Figure 1a). One site is in the seasonal upwelling region (CCE2), and the other is further offshore, within the core of the California Current (CCE1). The present study aims to analyze and quantify the seasonal variability of $pCO_{2,sw}$ and air-sea CO_2 flux between 2008 and 2022 in these two contrasting environments, identifying the underlying controlling processes. Our long time series of CO_2 fluxes also show pronounced interannual variability (Figures 1b and 1c). Therefore, another goal is to assess the interannual variability of pCO_2 and air-sea CO_2 flux between the nearshore and open-ocean regions and to test whether these long-term anomalies are related to interannual variability modes such as ENSO and MHWs.

2. Data and Methods

2.1. Physical and Carbon Observations

Long-term moored observations for physical and biogeochemical properties have been collected since 2008 (for CCE1) and 2010 (for CCE2) in the SCCS (project website: https://mooring.ucsd.edu/cce; Figure 1). The open-ocean CCE1 mooring is located 220 km southwest of Point Conception, California, in 4,100 m depth, predominantly within the core of the California Current (Lynn & Simpson, 1987). The CCE2 mooring is situated within the upwelling region on the continental slope in 800 m depth, 35 km southwest of Point Conception. This study used data from 11 November 2008 (at CCE1) and from 1 January 2010 (at CCE2) until 31 December 2022. The two moorings are co-located with line 80 of the California Cooperative Oceanic Fisheries Investigations (CalCOFI) at stations 80.80 (33°28.98′N, 122°31.98′W; CCE1) and 80.55 (34°19.02′N, 120°48.12′W; CCE2) (Bograd et al., 2003). Mooring locations were within 0.1° in latitude and longitude of the respective CalCOFI stations. Both moorings are maintained by the Ocean Time Series Group and the California Current Ecosystem Long-Term Ecological Research project based at Scripps Institution of Oceanography. The NOAA Pacific Marine Environmental Laboratory provides the surface CO_2 systems for the surface buoys of the moorings.

The surface buoys include an autonomous pCO_2 system ($MAPCO_2$; Battelle Memorial Institute; Sutton et al., 2014) and a Sea-Bird Electronics SBE16 SeaCAT, which records SST and sea surface salinity (SSS). An early version of the $MAPCO_2$ system was initially developed by Friederich et al. (1995) and includes an automated equilibrator-based system paired with a nondispersive infrared gas analyzer (LI-COR, model LI-820) that is calibrated in situ before each measurement with a reference gas traceable to World Meteorological

Organization standards (Sutton et al., 2014). The system collects measurements of the CO_2 molar fraction (xCO_2) at the sea surface (~0.5 m below sea surface) and near-surface atmosphere (~1.5 m above sea surface) on a three-hourly basis. These measurements are converted to $pCO_{2,sw}$ and $pCO_{2,air}$ following Sutton et al. (2014). The associated uncertainty of the MAPCO$_2$ measurements is <2 µatm for $pCO_{2,sw}$, <1 µatm for $pCO_{2,air}$, while Sea-Bird SBE16 uncertainties are <0.01°C for SST, and <0.05 for SSS (Sutton et al., 2014, 2019; Tamburri et al., 2011; Vandemark et al., 2011). The final quality-controlled pCO_2 time series is available at Sutton et al. (2019).

2.2. Computation of Total Alkalinity

Total Alkalinity (TA) and salinity measurements from discrete water samples collected in the upper 10 m during the deployment and recovery cruises (Send et al., 2016, 2022) and from CalCOFI cruises (available at https://calcofi.org; last access on 22 April 2022) at stations 80.80 (CCE1) and 80.55 (CCE2) were used to derive a multiparametric relationship between TA, salinity, and temperature. TA-SSS relationships have been widely applied at the surface worldwide (e.g., Jiang et al., 2014; Lee et al., 2006; Millero et al., 1998), particularly in open ocean regimes because salinity changes account for over 80% of the surface TA variability (Millero et al., 1998). However, in coastal regimes, TA-SSS relationships may not perform as effectively as they do in open oceans due to additional processes such as upwelling, riverine inputs, and biological factors that make TA variability significantly more complex (e.g., Cai et al., 2010; Hunt et al., 2021). Our tests with water samples collected at both sites indicate that a fit using salinity and temperature as the input parameters yielded slightly lower uncertainties (RMSE of 3.38 and 3.28 µmol kg^{-1} at CCE1 and CCE2, respectively) than using solely salinity at the CCE sites (see Text S1, Tables S1–S2, and Figure S1 in Supporting Information S1) or previous estimations from Gray et al. (2011) in the CCS. The resulting fits to estimate TA follow the format of Alin et al. (2012) for the CCS and are at each mooring:

$$\mathrm{TA}_{\mathrm{CCE1}} = 2220 + 51.27 \times (\mathrm{SSS} - S_{\mathrm{ref,CCE1}}) + 0.7684 \times (\mathrm{SST} - T_{\mathrm{ref,CCE1}}) - 3.177 \times [(\mathrm{SSS} - S_{\mathrm{ref,CCE1}})(\mathrm{SST} - T_{\mathrm{ref,CCE1}})] \quad (1)$$

$$\mathrm{TA}_{\mathrm{CCE2}} = 2238 + 59.88 \times (\mathrm{SSS} - S_{\mathrm{ref,CCE2}}) + 0.4847 \times (\mathrm{SST} - T_{\mathrm{ref,CCE2}}) - 4.788 \times [(\mathrm{SSS} - S_{\mathrm{ref,CCE2}})(\mathrm{SST} - T_{\mathrm{ref,CCE2}})] \quad (2)$$

where $S_{\mathrm{ref,CCE1}} = 33.20$ and $S_{\mathrm{ref,CCE2}} = 33.51$ are the mean salinity, and $T_{\mathrm{ref,CCE1}} = 15.34$°C and $T_{\mathrm{ref,CCE2}} = 14.62$°C are the mean temperature at the upper 10 m water column at the CCE1 and CCE2 mooring locations, respectively. The R^2 for CCE1 is 0.88, and for CCE2 it is 0.93.

2.3. Computation of DIC Using CO2SYS

DIC was calculated from the measured temperature, salinity, $pCO_{2,sw,}$ silicic acid, phosphate, and estimated TA at the surface using the CO2SYS v2 algorithm in Matlab® (Lewis & Wallace, 1998; Van Heuven et al., 2011). Silicic and phosphate concentrations were determined as the average surface concentration at each site using CalCOFI water samples (available at https://calcofi.org; last accessed on 22 April 2022). The constants used in CO2SYS v2 are carbonic acid dissociation constants from Mehrbach et al. (1973), refitted by Dickson and Millero (1987), along with the bisulfate dissociation constant of Dickson (1990a). Boric acid dissociation constant is from Dickson (1990b), and the borate to salinity ratio from Uppstrom (1974). Considering the sources of uncertainty, that is, errors in TA estimation and associated pCO_2 measurements, as well as the uncertainties associated with the constants used, the computed propagated uncertainty of surface DIC is estimated to be 6.12 µmol kg^{-1} at CCE1 and 5.71 µmol kg^{-1} at CCE2 (Orr et al., 2018). DIC was salinity normalized (indicated by nDIC) to the average surface salinity of the time series at CCE1 and CCE2 (Table 1) to account for dilution/concentration from the addition/removal of freshwater. The moorings also have pH sensors, but we concluded that the highest accuracy in carbon variables was obtained using the pair TA-pCO_2 rather than pCO_2-pH (Text S2, Figures S2 and S3 in Supporting Information S1).

Table 1
Statistics of the Daily-Averaged Time-Series Measurements at the CCE Moorings Calculated Between 2008 and 2022 (CCE1) and 2010 and 2022 (CCE2)

	CCE1 mooring (2008–2022)					CCE2 mooring (2010–2022)					
	Mean	Min	Max	Std	stE (NDF)	Mean	Min	Max	Std	stE (NDF)	"unbiased" mean
$pCO_{2,sw}$ (µatm)	390.0	329.3	549.4	22.7	4.1 (30)	398.2	223.7	759.8	57.3	5.2 (121)	393.4
$pCO_{2,air}$ (µatm)	398.0	368.1	431.9	11.1	5.0 (5)	401.6	368.2	434.1	11.7	5.2 (5)	N.A.
SST (°C)	16.03	12.09	20.78	1.74	0.29 (36)	14.49	10.28	21.81	1.83	0.27 (47)	14.78
F_{CO_2} (molC m^{-2} $year^{-1}$)	−0.52	−6.25	8.70	1.28	0.16 (63)	0.56	−6.88	40.31	4.03	0.32 (160)	0.23
SSS	33.18	32.28	33.73	0.21	0.05 (19)	33.46	32.58	33.90	0.21	0.05 (16)	N.A.
Chl-a (mg m^{-3})	0.33	0.05	1.49	0.19	0.02 (59)	1.25	0.15	6.63	0.92	0.08 (124)	1.19
nDIC (µmol kg^{-1})	2006.5	1970.4	2068.0	11.2	1.8 (38)	2029.5	1907.5	2140.7	30.7	3.62 (72)	2027
Wind speed (m s^{-1})	7.5	0.7	17.1	2.9	0.1 (858)	7.4	0.6	18.4	3.1	0.1 (1764)	7.31
ΔpCO_2 (µatm)	−7.9	−71.5	159.5	24.0	3.7 (41)	−3.4	−176.7	346.7	55.0	4.6 (142)	−7.2

Note. For the stE calculation, the number of degrees of freedom (NDF; in parenthesis) was calculated by dividing the length of the time series by the integral time scales of each parameter. The integral time scales were estimated as the integral over the autocorrelation function up to the first zero-crossing. "Unbiased" mean represents the best guess of the properties' mean excluding the influence of ENSO and PDO (for more details please see Section 3.3). N.A., not applicable; Std, standard deviation; stE, standard error of the mean.

2.4. Thermal and Non-Thermal Components of pCO_2 Seawater

To isolate the thermodynamic ($pCO_{2,sw}^{thermal}$) and non-thermal ($pCO_{2,sw}^{non\text{-}thermal}$) processes affecting seawater pCO_2 variability, we followed the decomposition proposed by Takahashi et al. (1993) at the CCE1 and CCE2 sites (Equations 3 and 4, respectively):

$$pCO_{2,sw}^{thermal} = pCO_{2,sw}^{mean} \times \exp(0.0423 \times (T_{obs} - T_{mean})) \quad (3)$$

$$pCO_{2,sw}^{non\text{-}thermal} = pCO_{2,sw}^{obs} \times \exp(0.0423 \times (T_{mean} - T_{obs})) \quad (4)$$

where $pCO_{2,sw}^{obs}$ is the observed surface pCO_2 seawater and pCO_2^{mean} is the mean observed surface pCO_2 seawater over the study period (CCE1: 390.27 ± 22.76 µatm; CCE2: 399.45 ± 57.80 µatm). T_{obs} and T_{mean} are the in situ SST and respective mean (CCE1: 16.02 ± 1.76°C; CCE2: 14.50 ± 1.85°C) at each site. We verified that processing the thermal and non-thermal effects through CO2SYS v2 (e.g., Williams et al., 2018; Wolfe et al., 2023) gave very similar results, and they would not have changed any of the conclusions drawn in the present analysis.

2.5. Air-Sea CO_2 Fluxes Calculation

Air-sea CO_2 fluxes (F_{CO_2}) were calculated using Equation 5:

$$F_{CO_2} = k \times K_0 \times \Delta pCO_2 \quad (5)$$

where $k = 0.251 \times U^2(Sc/660)^{-1/2}$ is the gas transfer velocity using a square dependence on wind speed at 10 m (U^2), Schmidt number (Sc, calculated as a function of SST), and a scaling factor of 0.251 adapted for Cross-Calibrated Multi-Platform (CCMP) winds (Wanninkhof, 2014). K_0 is the solubility coefficient for CO_2 (Weiss, 1974), and $\Delta pCO_2 = pCO_{2,sw} - pCO_{2,air}$ is the difference in pCO_2 atmosphere and surface-ocean CO_2.

To calculate air-sea F_{CO_2} at the CCE moorings, we computed daily averages of ΔpCO_2 and used daily winds at 10 m height from the CCMP V3.1 wind speed data (Mears et al., 2022), which is the same wind product that Wanninkhof (2014) used to derive the $0.251 \times U^2$ relationship. The uncertainty of the calculated F_{CO_2} is approximately 20%, primarily attributed to the uncertainty of gas transfer velocity k, which includes uncertainties in the wind estimates (Wanninkhof, 2014). The moorings are also equipped with a meteorological station that measures wind speed. We also estimated the F_{CO_2} using the mooring winds (adjusted to 10 m height using Equation 1 in Sutton et al. (2017)), and the F_{CO_2} magnitude is in the same order as the one presented here. The sign

of ΔpCO_2 determines the direction of the F_{CO_2}; a positive F_{CO_2} indicates a flux into the atmosphere or "source" ($pCO_{2,sw} > pCO_{2,air}$) while a negative F_{CO_2} indicates a flux into the ocean or "sink" ($pCO_{2,sw} < pCO_{2,air}$).

2.6. Anomaly Time Series Calculation and Trends Estimation

The anomaly time series were computed by subtracting the daily climatological average at each mooring (calculated from all years of the mooring record) from the observed daily value. For example, all 1 January measurements were averaged (1 January climatology) and subtracted to the observed variable at each 1 January. These anomalies will be denoted with a δ.

The resulting de-seasonalized (or anomaly) time series were also fitted using a least squares regression to estimate the linear trends for the study period. Linear regression and uncertainties associated with the trends were estimated following Glover et al. (2011; Chapter 3).

2.7. Determination of Marine Heatwave Periods

The occurrence of marine heatwaves at the CCE moorings was determined following the methodology of Hobday et al. (2016). The authors defined MHW as an anomalous warm event of at least five or more days where the SST is warmer than the 90th percentile based on a 30-year climatology. We used the high-resolution daily Optimum Interpolation Sea Surface Temperature (OISST) v2 data set (Huang et al., 2021) provided by the National Oceanic and Atmospheric Administration (NOAA) to estimate the SST climatology at the closest points to the nominal mooring positions between 1 January 1981 and 31 December 2022. To determine the suitability of the OISST data set for determining the climatology and the 90th percentile departure from climatology, we compared the SST from the NOAA OISST V2 and the moorings' SST during the overlapping periods (Figure S4 in Supporting Information S1). The results of this comparison demonstrated a high degree of correlation between the two time series ($r = 0.96$ at CCE1 and $r = 0.95$ at CCE2).

In this study, we were interested in gaining insight into the effects of MHW on $pCO_{2,sw}$ and F_{CO_2}. To this end, we used data from those MHW months with a minimum of 75% (or 22.5 days) of valid $pCO_{2,sw}$ measurements. The starting and ending dates of the MHW Blob 1.0 are provided in Text S3 in Supporting Information S1.

2.8. Ancillary Data

Surface chlorophyll *a* (Chl-a) estimates between 2008 and 2022 are from a merged 4 km resolution data set optimized for the CCS region, as described in Kahru et al. (2012, 2015). This product integrates surface Chl-a data from five satellite ocean color sensors (Ocean Color and Temperature Scanner, Sea-Viewing Wide Field-of-View Sensor, Medium-Resolution Imaging Spectrometer, Moderate Resolution Imaging Spectroradiometer A, and Visible Infrared Imaging Radiometer Suite). Here, we used a 5-day running mean Chl-a at the surface extracted in a square of 3×3 pixels around the closest point of the CCE moorings sites (https://spg-satdata.ucsd.edu/CC4km/). The Chl-a was area-averaged and compared with CalCOFI surface water samples collected at the CCE moorings sites and analyzed by fluorometry before and after acidification (Figure S5 in Supporting Information S1). The 5-day running mean Chl-a product correlated well with CalCOFI surface water samples at the CCE1 ($R^2 = 0.90$) but underestimated the surface Chl-a at the CCE2 site ($R^2 = 0.58$).

To delineate the periods of El Niño and La Niña at the CCE sites, we used the revised Multivariate ENSO Index Version 2 (MEI.v2; https://www.psl.noaa.gov/enso/mei/). For this study, only periods of strong El Niño (MEI > 1.5) and strong La Niña (MEI < −1.5) are considered. The start and ending dates of each strong episode are reported in Text S3 in Supporting Information S1. In addition to the MEI index, we used the North Pacific Gyre Oscillation (NPGO; Di Lorenzo et al., 2008) and the Pacific Decadal Oscillation (PDO; Mantua & Hare, 2002) to investigate potential correlations with the interannual variability of $pCO_{2,sw}$ and F_{CO_2} between 2008 and 2022.

3. Results and Discussion

3.1. Daily-Averaged Statistics at the CCE Moorings Between 2008 and 2022

The statistics of the daily records, including mean, minimum, maximum, and standard deviation, at each CCE mooring are summarized in Table 1. Since our records sometimes contain substantial gaps, we tested several

methods to remove potential biases due to uneven sampling of seasons or months. We also tried filling the gaps with respective climatological daily values. None of these tests gave significantly different results than those described below.

It is surprising at first sight that at CCE2, the average ΔpCO_2 over the entire record (2010−2022) is negative (−3.4 μatm; Table 1). While the mean air-sea F_{CO_2} is positive, if we estimate the mean F_{CO_2} using the average values of each term in Equation 5 for the entire period, then this would imply that the mean air-sea F_{CO_2} is negative. It turns out that the co-variability between the ΔpCO_2 and the wind in Equation 5 leads to high fluxes, outweighing the negative values resulting from using just the means of each term in Equation 5 (Song et al., 2025). While in our case, most of the covariance comes from upwelling event time-scales, this effect is similar to the seasonal co-variability between wind and undersaturation creating a mean gas flux in the Mid-Atlantic Bight as explained by DeGrandpre et al. (2002).

3.2. Mean Seasonal pCO_2 and Air-Sea F_{CO_2}

The mean annual cycles of surface $pCO_{2,sw}$, air-sea F_{CO_2}, nDIC and DIC concentration, SST, SSS, and Chl-a concentration at the CCE moorings are illustrated in Figure 2. These sites reflect the characteristics of open-ocean (CCE1) and seasonal upwelling regimes (CCE2). The ranges of the annual cycles are larger at the upwelling site due to the seasonal upwelling of CO_2-rich waters from beneath the thermocline.

3.2.1. Mean F_{CO_2} in Open-Ocean and Upwelling Regimes

The annual mean air-sea F_{CO_2} at the CCE1 site is −0.52 molC m^{-2} $year^{-1}$ (Table 1; Figure 2c), implying that this open-ocean site acts as a CO_2 sink. CO_2 uptake is observed for much of the year, except in summer (July to October; Figure 2c). The seasonal variability of F_{CO_2}, defined as the range of the annual cycle, is 2.45 molC m^{-2} $year^{-1}$ and is mainly explained by ΔpCO_2 ($r > 0.90$). Wind speed plays a minor role in the air-sea F_{CO_2} ($r = -0.09$).

The CCE2 site behaves as a CO_2 source, with a net annual air-sea F_{CO_2} of 0.56 molC m^{-2} $year^{-1}$ over the observed years (Figure 2d) and a seasonal range of 6.40 molC m^{-2} $year^{-1}$. CO_2 outgassing occurs typically between March and July, coinciding with the strong upwelling season in the SCCS (Jorgensen et al., 2024). Upwelling brings high-CO_2 and nutrient-rich waters to the surface, favoring CO_2 outgassing (Figure 2, right panels). The observed high variability (expressed as the standard deviation of the mean) during these months is due to the interannual differences in the timing, intensity, and duration of the upwelling events and season (Bograd et al., 2009). After upwelling, a seasonal relaxation phase follows, during which the growing water column stratification prevents CO_2-rich water from reaching the surface.

The annual mean air-sea F_{CO_2} at the CCE moorings fall within the ranges reported in the CCS (Fiechter et al., 2014; Hales et al., 2012; Takahashi et al., 2009; Turi et al., 2014). The net annual F_{CO_2} for CCE1 is one of the lowest reported among moorings in the North Pacific (Sutton et al., 2017). Interestingly, Wolfe et al. (2023) reported that station 90.90 of CalCOFI, located some 440 km offshore, "appears to be an annual net source of CO_2 to the atmosphere" even though this would normally be considered an open-ocean (non-coastal) site. One possible explanation is that station 90.90 lies near the edge of a zero-F_{CO_2} contour in the CCS (their figure 3 shows a balance between $pCO_{2,air}$ and $pCO_{2,atm}$). Our value for the mean CO_2 outgassing at CCE2 (and also the unbiased value discussed later) is of the same order of magnitude as in situ observations and model outputs in the coastal upwelling region of the CCS (Borges et al., 2005; Leinweber et al., 2009; Pennington et al., 2010).

The air-sea F_{CO_2} reported here at CCE2 was initially calculated over the observational period of 2010–2022. The prevalence of El Niños and La Niñas in different years may lead to a bias, depending on how many of these anomalous years are included in the average. For example, Song et al. (2025) use the years 2011–2020 and get a much smaller (but still positive) mean F_{CO_2} for the CCE2 timeseries. In Section 3.3, we discuss how interannual modes, such as ENSO and PDO, affect the mean value of air-sea F_{CO_2}, and suggest a method to correct for the resulting bias.

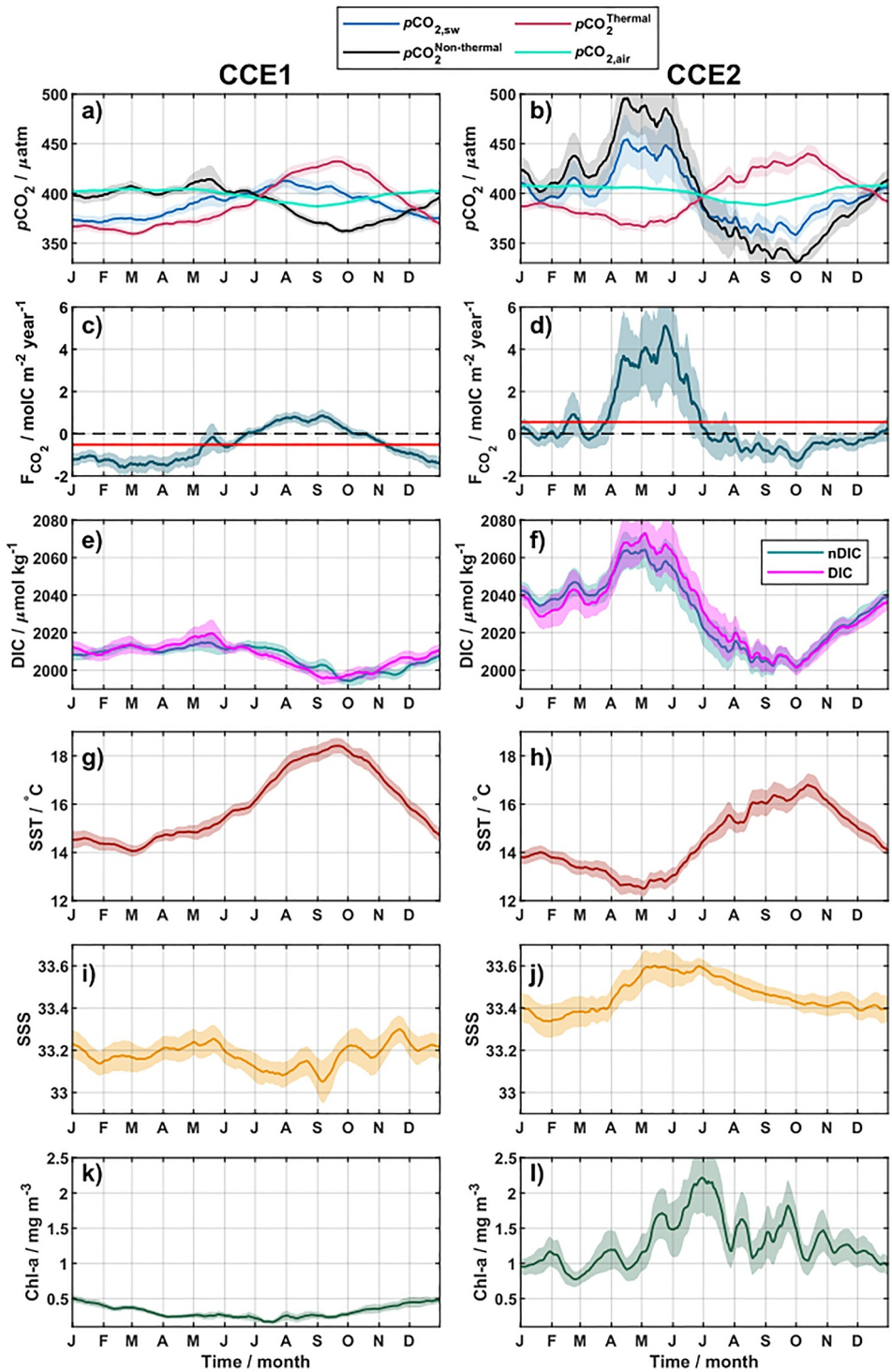

Figure 2. Annual cycles at CCE1 (offshore; left panels) and CCE2 (upwelling; right panels). (a–b) $pCO_{2,sw}$ (partial pressure of carbon dioxide in seawater; in blue), $pCO_{2,air}$ (partial pressure of carbon dioxide in the atmosphere; in cyan), and $pCO_{2,sw}$ decomposition into thermal (dark pink) and non-thermal (black) components. (c–d) Air-sea CO_2 fluxes (F_{CO_2}): black dashed line marks zero F_{CO_2}; red solid lines are each site's net annual mean F_{CO_2}. (e–f) Salinity-normalized dissolved inorganic carbon (nDIC) concentration (blue) and surface DIC (magenta). (g–h) Sea surface temperature; (i–j) Sea surface salinity; (k–l) Satellite-estimated chlorophyll *a* (Chl-a) concentration at the surface. Shadowed areas in all panels represent the standard error of the mean. Annual cycles were calculated for 2008–2022 at CCE1 and 2010–2022 at CCE2.

3.2.2. Drivers of Seasonal $pCO_{2,sw}$ and nDIC in the Open-Ocean Regime

The observed $pCO_{2,sw}$ follows the same seasonal pattern as SST (Figure 2g), with higher values in summer and lower values in winter ($r = 0.93$), opposite to the phase of $pCO_{2,air}$ (Figure 2a). The decomposition of the measured $pCO_{2,sw}$ (Equations 3 and 4) reveals that $pCO_{2,sw}^{thermal}$ follows the SST annual cycle, whereas the $pCO_{2,sw}^{non\text{-}thermal}$ resembles the nDIC annual cycle ($r = 0.97$; Figures 2a and 2e). The observed seasonal range for $pCO_{2,sw}$ is 54 µatm, with both $pCO_{2,sw}$ components having comparable ranges (81 µatm for $pCO_{2,sw}^{thermal}$ and 64 µatm for $pCO_{2,sw}^{non\text{-}thermal}$). Although the non-thermal component is not small, its phasing and amplitude are such that the overall $pCO_{2,sw}$ curve follows more the thermal component and is largely out of phase with the non-thermal part.

The opposite phase of SST and nDIC seasonal cycles at the CCE1 site aligns with observations at other sites in the North Pacific (Dore et al., 2003; Sutton et al., 2017; Wolfe et al., 2023; Xiu & Chai, 2014). The nDIC annual cycle fluctuates by 27 µmol kg^{-1}, peaking during winter and reaching lower values in summer (Figure 2e), opposite to the air-sea F_{CO_2} (Figure 2c). The seasonal nDIC qualitatively follows the expected pattern from a relationship between water-mass density and DIC. In particular, the deepening of the mixed layer in late fall and winter mixes underlying dense, CO_2-rich water upward, thus increasing surface nDIC (Figure S6 in Supporting Information S1). In spring and summer, air-sea F_{CO_2} modulates the purely density-predicted nDIC, initially raising it through CO_2 uptake before reducing it due to CO_2 outgassing. The increase in nDIC during winter is not as strong as the cooling effect on $pCO_{2,sw}$, and only partly offsets the temperature effect (see $pCO_{2,sw}$ observed and their components in Figure 2a; Ishii et al., 2014; Takahashi et al., 2002).

3.2.3. Drivers of Seasonal $pCO_{2,sw}$ and nDIC in the Upwelling Regime

At the CCE2 site, the observed $pCO_{2,sw}$ reflects the nDIC seasonal cycle, with higher values in spring due to the vertical advection of CO_2-rich water into the upper water column during the upwelling season. This increases $pCO_{2,sw}$, and DIC at the surface. During the relaxation phase, primary production consumes inorganic carbon, lowering $pCO_{2,sw}$ and DIC (Figure 2f). The detailed annual cycles we constructed show that in this regime, the thermal component is opposite to the observed $pCO_{2,sw}$ and air-sea F_{CO_2}. However, the $pCO_{2,sw}^{non\text{-}thermal}$ mirrors the nDIC seasonal cycle, which dominates and determines the seasonal shape of pCO_2 and the air-sea F_{CO_2} (Figures 2b and 2f). The observed annual peak-to-peak range for $pCO_{2,sw}$ is 142 µatm while the $pCO_{2,sw}^{thermal}$ is 74 µatm and $pCO_{2,sw}^{non\text{-}thermal}$ is 165 µatm. This observation further reinforces that non-thermal processes drive the seasonality of $pCO_{2,sw}$ at the CCE2 site, similar to the results of Chen and Hu (2019).

3.3. Inter-Annual Variability of $pCO_{2,sw}$ and CO_2 Fluxes Anomalies

On inter-annual timescales, the annual mean net air-sea F_{CO_2} at CCE1 for individual years ranged from −0.97 molC m^{-2} $year^{-1}$ in 2010 to 0.22 molC m^{-2} $year^{-1}$ in 2015 (i.e., averages over the years which are plotted as thin blue lines in Figure 3c). At CCE2, this varied between −0.66 molC m^{-2} $year^{-1}$ in 2015 to 1.88 molC m^{-2} $year^{-1}$ in 2021. The interannual variability of the air-sea F_{CO_2}, determined by the standard deviation of the annual-mean F_{CO_2} across the years with over 300 days of measurements (7 years total for each mooring), was 0.27 molC m^{-2} $year^{-1}$ at CCE1 and 0.92 molC m^{-2} $year^{-1}$ at CCE2.

To study interannual variability, we examined the anomaly time series (δpCO_2, δF_{CO_2}, δnDIC, etc.) by removing the influence of the respective mean seasonal cycles (Figures 3 and 4, right panels). We then explored the differences between open-ocean and upwelling regimes along CalCOFI line 80, focusing on how other (non-seasonal) processes impact the surface carbonate system in the SCCS region.

The variability of $\delta pCO_{2,sw}$ and δFCO_2 (expressed as the standard deviation of the time series in Figures 3 and 4) is greater at CCE2 (51 µatm and 3.7 molC m^{-2} $year^{-1}$, respectively) compared with CCE1 (19 µatm and 1 molC m^{-2} $year^{-1}$, respectively). This difference reflects the more dynamic CCE2 site, characterized by strong interannual variability with respect to the occurrence (and strength) or absence of seasonal upwelling (Lowcher, 2023), compared with the open-ocean site. The $\delta\Delta pCO_2$ controls the δF_{CO_2} at both sites, with the surface wind anomalies exerting less impact at CCE1 and only indirectly influencing the air-sea F_{CO_2} magnitude through wind-driven upwelling at CCE2.

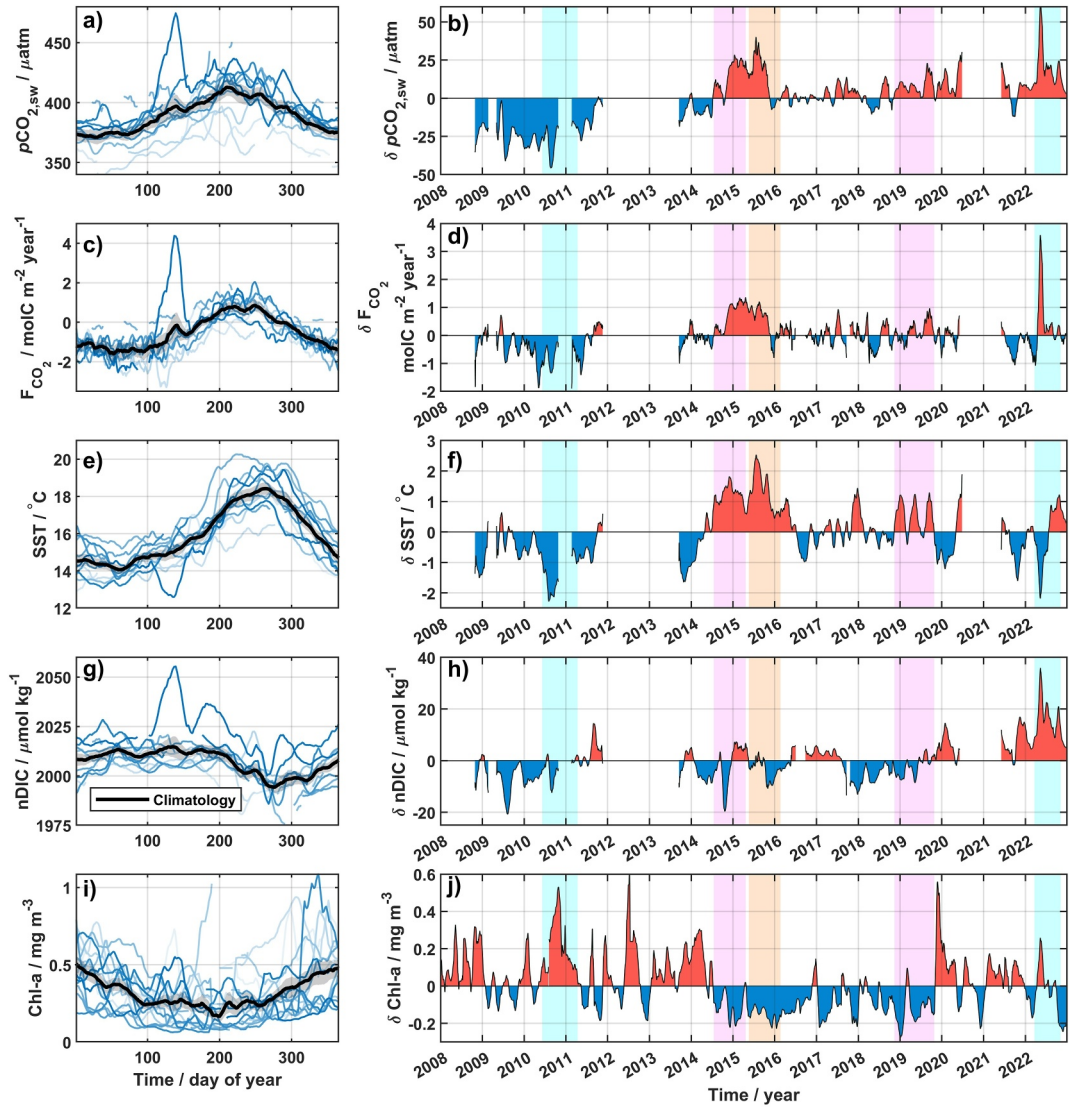

Figure 3. CCE1 site: seasonal (left panels) and respective anomaly (δ) time series (right). From top to bottom, the variables are partial pressure of CO_2 in seawater ($pCO_{2,sw}$; a–b), CO_2 flux (F_{CO_2}; c–d), sea surface temperature (SST; e–f), salinity-normalized DIC (nDIC; g–h), and satellite-derived chlorophyll *a* concentration at the surface (Chl-a; i–j). Solid black lines on the left panels represent the annual mean cycle between 2008 and 2022 (same as Figure 2), and the thin blue lines show individual years (the color scale is progressively darker from the early years (2008) to recent years (2022)). Cyan shaded periods on the right panels represent strong La Niña periods; magentas are the MHWs known as Blob 1.0 (in 2015/2016) and the warm anomaly period in 2018/2019 (Lowcher, 2023). Orange represents the strong 2015/2016 El Niño period. All time series on the right panels are smoothed with a 30-day running mean.

At the CCE2 site, periods of intense upwelling are readily distinguishable in $\delta pCO_{2,sw}$ and δF_{CO_2} as red-filled positive phases (Figures 4b and 4d). Most of the positive $\delta pCO_{2,sw}$, δF_{CO_2}, δnDIC, and δChl-a at the surface are linked to upwelling, with the years 2010–2013 and 2021–2022 standing out. In contrast, from 2014 to 2020, δFCO_2 and δChl-a at the surface were predominantly negative (Figure 4). This period coincided with a positive along-shore wind stress anomaly ($\delta\tau$, Figure 4h), indicating less favorable conditions for upwelling, which we believe explains the observed negative anomalies. The depth of the 25.5 kg m^{-3}-isopycnal was used as a proxy for upwelling at line 80 of CalCOFI (Rudnick et al., 2017), and this correlates with ΔpCO_2 and the air-sea F_{CO_2} (Figure S7 in Supporting Information S1).

The relationship between the major modes of climate variability and the full records of daily time series of $\delta pCO_{2,sw}$ and δF_{CO_2} are presented in Table S3 in Supporting Information S1. Although overall correlations at the

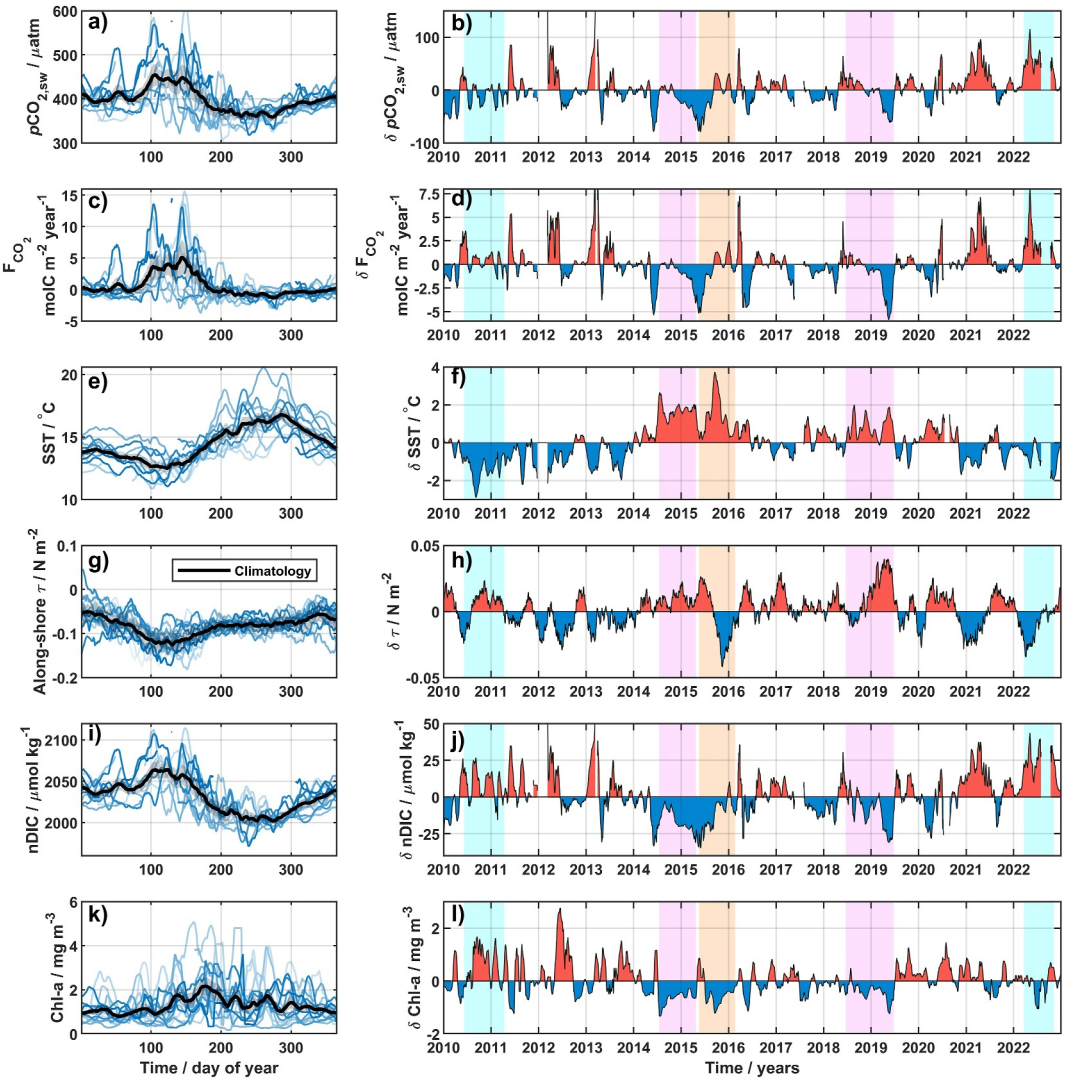

Figure 4. CCE2 site: seasonal (left panels) and respective anomaly (δ) time series (right). From top to bottom, the variables are partial pressure of CO_2 in seawater ($pCO_{2,sw}$; a–b), CO_2 flux (F_{CO_2}; c–d), sea surface temperature (SST; e–f), along-shore wind stress (τ; g–h), salinity-normalized DIC (nDIC; i–j), and satellite-derived chlorophyll *a* concentration at the surface (Chl-a; k–l). Solid black lines on the left panels represent the annual mean cycle between 2010 and 2022 (same as Figure 2), and the thin blue lines show individual years (the color scale is progressively darker from the early years (2010) to recent years (2022)). Cyan shadowed periods on the right panels represent strong La Niña periods; magentas are the MHWs known as Blob 1.0 (in 2015/2016) and the warm anomaly period in 2018/2019 (Lowcher, 2023). Orange represents the strong El Niño of 2015/2016. Anomaly time series are smoothed with a 30-day running mean filter, except for wind speed, for which we used a 90-day running mean.

CCE moorings and in the North Pacific are weak (Valsala et al., 2012), it is apparent that the sense of the correlation at the CCE moorings is opposite for the same index. At the open-ocean site, NPGO shows the strongest negative correlations with both $\delta pCO_{2,sw}$ and the δF_{CO_2}. At CCE2, the highest correlation is found between PDO and δF_{CO_2} and $\delta pCO_{2,sw}$ time series. Positive PDO phases are associated with anomalously warm SST and suppressed upwelling along the U.S. West Coast (Jacox et al., 2015; Mantua & Hare, 2002). Suppressed upwelling is linked to a negative δF_{CO_2}, explaining the negative correlation observed at this site, supporting findings by Brady et al. (2019). Despite the low correlations using the full anomaly timeseries, our findings at the CCS region align with Xiu and Chai's (2014) conclusions regarding the influence of PDO and NPGO on air-sea F_{CO_2} year-to-year variability. The weaker correlations calculated with PDO compared with those with NPGO at our

sites may be related to the fact that the NPGO influence is stronger south of 38°N compared with the PDO (Chhak & Di Lorenzo, 2007; Di Lorenzo et al., 2008).

The interannual variability of annual-mean quantities, however, is strongly correlated with ENSO and PDO at CCE2. We computed yearly averages of air-sea F_{CO_2}, pCO_2, SST, SSS, nDIC, and ΔpCO_2 and compared these with annual means of the ENSO and PDO indexes of the corresponding years. Scatter plots of these annual climate indexes versus air-sea F_{CO_2} are shown in Figure S11 in Supporting Information S1. We can use this relation to "normalize" the average annual F_{CO_2} (and the other variables) against these indexes by fitting a least-square regression line and reporting the expected value for neutral conditions (or zero index) from these regressions (Table 1; Tables S4 and S5 in Supporting Information S1). We call this the unbiased mean, and in Table 1, we report the average values calculated from the expected neutral ENSO and neutral PDO. The average F_{CO_2} for a neutral ENSO is 0.19 ± 0.19 molC m^{-2} $year^{-1}$ while F_{CO_2} for a neutral PDO is 0.26 ± 0.14 molC m^{-2} $year^{-1}$ (Table 1). We conclude that our average air-sea F_{CO_2} (0.56 molC m^{-2} $year^{-1}$) is biased by the prevalence of strong La Niñas and cold phases PDO in our record (Figure S11 in Supporting Information S1). No correlations were found between annual averages and PDO (or ENSO) at the open-ocean site (not shown).

Both sites show multi-year periods of predominantly positive and negative anomalies, indicative of processes that substantially disrupted the normal seasonal cycle at these sites (Figures 3 and 4, right panels). The outstanding events in these periods correspond to the North Pacific Warm Anomaly (or Blob 1.0) followed by the strong 2015/2016 El Niño (Lilly et al., 2019), a warm anomaly in 2018/19 (Lowcher, 2023), and the strong La Niñas in 2010/2011 (Todd et al., 2011) and 2022. They are highlighted with shading in Figures 3 and 4 and are discussed below. The only period with an annual-mean positive air-sea F_{CO_2} (0.22 molC m^{-2} $year^{-1}$) at the open-ocean site coincided with the Blob 1.0 event and the 2015/2016 El Niño onset.

3.3.1. Impact of La Niñas in the Open-Ocean Regime

During the 2010/2011 La Niña, a mean negative $\delta pCO_{2,sw}$ of −27 µatm was observed (Figure 5a), a result of the presence of colder waters at the surface (average δSST of −1.49°C; Figure 3). This colder water ($\delta pCO_{2,sw}^{thermal}$) contributed significantly to the observed negative $\delta pCO_{2,sw}$, accounting for a decrease of −22 µatm (81% of the total). $\delta pCO_{2,sw}^{non\text{-}thermal}$ processes contributed an additional −5 µatm (19%) to the overall $\delta pCO_{2,sw}$. Consequently, a net air-sea F_{CO_2} of −0.41 molC m^{-2} (uptake) was calculated in a 10-month period during the 2010/2011 La Niña.

The 2022 La Niña (Figure 5c) revealed striking differences from the 2010/2011 La Niña. The average observed $\delta pCO_{2,sw}$ was positive (+22 µatm), and a net air-sea F_{CO_2} of +0.31 molC m^{-2} (outgassing) was calculated during this 7-month event. $\delta pCO_{2,sw}^{non\text{-}thermal}$ drove the $\delta pCO_{2,sw}$ until August 2022, when summer SST warming overrode the non-thermal processes. In May 2022, an upwelling filament reached the open-ocean site (Figure 1), and its signature was seen in the surface outcrop of isopycnals (Figure S8c in Supporting Information S1): cold SST, anomalously high nDIC concentration (Figure 3h), and higher Chl-a concentration (Figure 5c). We consider this to be one factor contributing to the distinct nDIC signature of the 2022 La Niña compared with the 2010/2011 La Niña. In Section 3.4, we explore the potential influence of anthropogenic CO_2 uptake from 2010 to 2022 as an additional role in the anomalous high DIC concentration during the 2022 La Niña observed at the open-ocean site.

3.3.2. Impact of La Niñas in the Upwelling Regime

During both La Niña events at CCE2, we observed remarkably high nDIC concentration and a drop in SST (Figures 4f and 4j), as expected when upwelling brings CO_2-rich subsurface waters to the surface (see the isopycnals outcrop in Figures S8b and S8d in Supporting Information S1). However, the processes driving the variations in $\delta pCO_{2,sw}$ and δF_{CO_2} during 2010/2011 La Niña and 2022 La Niña were distinct.

In the 2010/2011 La Niña, the average $\delta pCO_{2,sw}$ was −10 µatm (Figure 5b), and the mean δSST was −1.48°C. This gives an average contribution from δSST of −23 µatm to the observed mean $pCO_{2,sw}$ while the $\delta pCO_{2,sw}^{non\text{-}thermal}$ contribution was +13 µatm. This suggests that the observed mean $\delta pCO_{2,sw}$ was controlled more by SST. In contrast, during the 2022 La Niña, the observed average $\delta pCO_{2,sw}$ was positive (+61 µatm), although the mean δSST remained negative (−0.80°C; Figure 4d). This cooling effect on $pCO_{2,sw}$ (−16 µatm) was greatly exceeded by the $pCO_{2,sw}^{non\text{-}thermal}$ contribution of +77 µatm. Despite the differing driving mechanisms of $\delta pCO_{2,sw}$

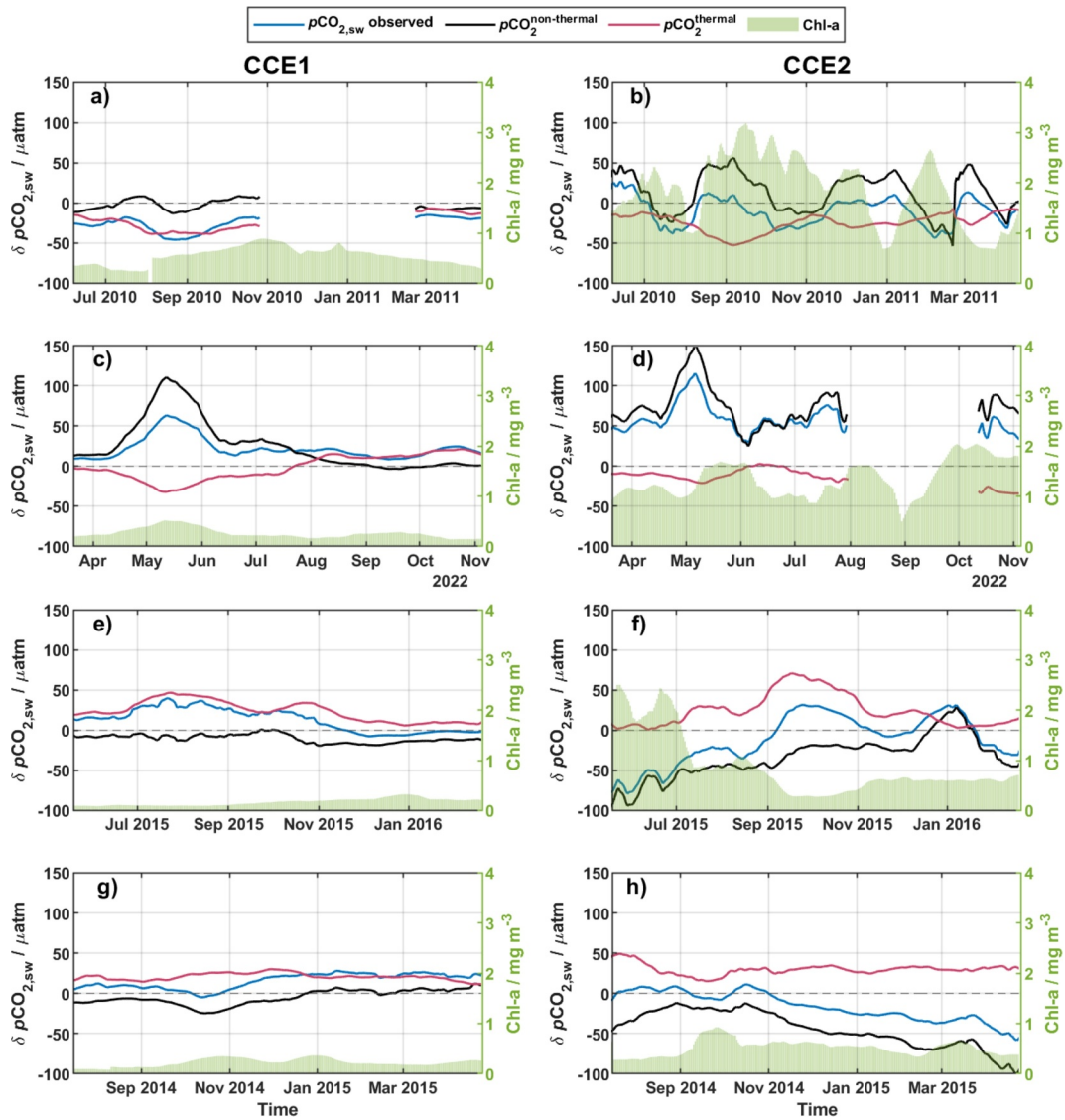

Figure 5. Anomaly of $pCO_{2,sw}$ and its components during major events marked in Figures 3 and 4. Anomaly of $pCO_{2,sw}$ measured (blue), thermal ($pCO_{2,sw}^{thermal}$; red), and non-thermal components ($pCO_{2,sw}^{non-thermal}$; black) of seawater pCO_2 during the (a–b) La Niña 2010/2011, (c–d) La Niña 2022, (e–f) El Niño 2015/2016, and (g–h) Blob 1.0 in 2014/2015. The anomaly time series (δ) were calculated as described in Section 2.6. Satellite-derived Chl-a concentrations at the surface during each event are plotted as green (concentrations in the right *y*-axis). The left and right panels show the different components of $pCO_{2,sw}$ at the CCE1 and CCE2 sites, respectively.

between the two events, both La Niña events showed a net air-sea F_{CO_2} outgassing: +0.31 molC m^{-2} released by the ocean over 10 months in 2010/2011 and +1.89 molC m^{-2} over 7 months in 2022. In the latter event, the CO_2 outgassed into the atmosphere was three times the normal annual carbon release. This is similar to Friederich et al. (2002), who reported an average F_{CO_2} of 1.9 molC m^{-2} $year^{-1}$ during the 1998–1999 La Niña in the Monterey Bay.

Throughout 2010/2011 La Niña, $\delta pCO_{2,sw}^{non-thermal}$ fluctuated between positive and negative values, reflecting a series of upwelling and relaxation events (Figure 5b and S8b). We suggest the following chain of events to explain these fluctuations: (a) Upwelling caused vertical water movement (seen as an outcropping of the isopycnals in Figure S5b in Supporting Information S1), resulting in a surplus of DIC (positive $\delta pCO_{2,sw}$) that exceeded $pCO_{2,air}$ causing CO_2 outgassing. (b) The influx of nutrient-rich waters fueled phytoplankton growth, increasing Chl-a at the surface; however, this effect was not immediate. First, we observed a relaxation of the water column

(as evidenced by the flattening of the isopycnals in Figure S8b in Supporting Information S1), followed by an increase in Chl-a at the surface (Figure 5b at the beginning of July 2010). (c) At this point, DIC was converted to organic carbon via primary production, decreasing $pCO_{2,sw}$. The chain of upwelling and relaxation events, spanning from days to weeks during the 2010/2011 La Niña (Figure S8b in Supporting Information S1), diminished the influence of $pCO_{2,sw}^{non\text{-}thermal}$ compared with the 2022 La Niña, where the isopycnals outcropped at the surface for a longer period (Figure S8d in Supporting Information S1).

3.3.3. Impact of El Niño in the Open-Ocean Regime

During the 2015/2016 El Niño, the observed $\delta pCO_{2,sw}$ (average of +13 µatm) was influenced by both $pCO_{2,sw}^{thermal}$ and $pCO_{2,sw}^{non\text{-}thermal}$ processes, with the thermal component dominating until November 2015 (Figure 5e). During the El Niño event, δSST averaged 1.35°C, contributing to an increase of $\delta pCO_{2,sw}$ of 24 µatm while $\delta pCO_{2,sw}^{non\text{-}thermal}$ decreased $\delta pCO_{2,sw}$ by −11 µatm. The high temperatures in the first half of El Niño led to strong stratification of the upper water column, reducing mixing with sub-surface waters rich in CO_2 (Figure S8e in Supporting Information S1) and causing a decrease in surface Chl-a concentration (and at 40 m; Lilly et al., 2019). CCE1 behaved as a CO_2 source during 2015/2015 El Niño, with a net CO_2 outgassing of 0.12 molC m^{-2}.

3.3.4. Impact of El Niño in the Upwelling Regime

At the onset of El Niño at CCE2, a high concentration of Chl-a at the surface (Figure 5f), which results in a deficit of DIC (hence, negative $\delta pCO_{2,sw}^{non\text{-}thermal}$), suggested that $pCO_{2,sw}$ was reduced due to enhanced primary production. The high Chl-a concentration was caused by an upwelling event between May and June 2015 (Figure S9 in Supporting Information S1), preceding the advent of the El Niño. However, during the 2015/2016 El Niño event, strong stratification (Figure S8f in Supporting Information S1) suppressed upwelling and deepened the nutricline (Lowcher, 2023), resulting in low Chl-a at the surface. The absence of upwelling led to an average $pCO_{2,sw}^{non\text{-}thermal}$ contribution of −34 µatm, resulting in a net air-sea F_{CO_2} of −0.30 molC m^{-2} during the 2015/2016 El Niño. Similar findings were observed by Friederich et al. (2002) during the 1997/1998 El Niño at station M1 in Monterey Bay, which was also associated with a suppressed upwelling observed in the region. It is, therefore, clear that non-thermal processes in coastal environments must be considered when modeling the drivers of interannual variability.

3.3.5. Impact of Marine Heatwaves in the Open-Ocean Regime

At CCE1, the Blob 1.0 event persisted for 279 days, significantly longer than this site's average MHW duration of 39 days. The $\delta\Delta pCO_2$ was positive during this event (similar to the positive anomaly in Figure 3b since $pCO_{2,air}$ had no notable anomaly) and controlled by the $pCO_{2,sw}^{thermal}$ (Figure 5g). An average δSST during Blob 1.0 of 1.24°C (peaking at 1.78°C) contributed to increased $pCO_{2,sw}$ by 5%, resulting in positive δF_{CO_2} (Figure 3). The average F_{CO_2} over the heatwave was 0.15 molC m^{-2} $year^{-1}$, resulting in a total net carbon outgassing of 0.12 molC m^{-2} across 10 months. Compared with the average annual F_{CO_2}, Blob 1.0 alone accounted for carbon outgassing equivalent to 30% of the typical CO_2 uptake observed within a year. Similarly, a positive $\delta pCO_{2,sw}$ was observed by Wolfe et al. (2023) at another CalCOFI open-ocean station (station 90.90) in the SCCS, as well as at various other moorings in the North Pacific (Sutton et al., 2017).

The CCE1 site experienced 23 months (13% of the observations) with MHWs. Over the 15-year record, each calendar-month at CCE1 experienced at least one MHW, except for May (Figure 6a). During months affected by MHWs at the open-ocean site, CO_2 uptake generally decreased, except in December 2015 and 2018. The F_{CO_2} magnitude decreased by up to 91% during MHWs for months with a climatological mean CO_2 uptake. As a result, air-sea F_{CO_2} was closer to zero (low CO_2 uptake), with instances of CO_2 outgassing in June, October, and November. Summer months, where CO_2 outgassing is observed, saw an intensification of CO_2 outgassing. SST ($pCO_{2,sw}^{thermal}$) was the main driver on $pCO_{2,sw}$ (and F_{CO_2}) at all observed MHWs. Wind speed influenced the F_{CO_2} magnitude; in 6 out of 23 cases, increasing wind speed correlated with increasing F_{CO_2} magnitude while F_{CO_2} decreased under low wind conditions in the other cases. This suggests that offshore wind can exacerbate the climatological observed air-sea F_{CO_2} in either direction. Edwing et al. (2024) observed similar behavior during lower wind speeds in the Mid- and South-Atlantic Bight. The authors noted that this results from MHWs driven by

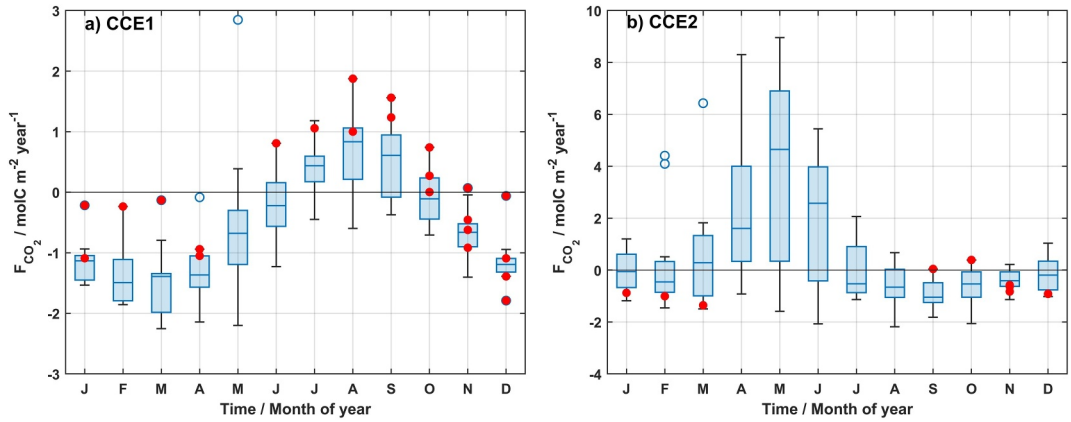

Figure 6. (a) Monthly air-sea F_{CO_2} during MHWs (red dots) at CCE1 and (b) CCE2. Box and whisker plots indicate the median, upper and lower quartiles, and minimum and maximum values that are not outliers for each month. The red dots correspond to months under the influence of MHW (details on the classification of a month under the influence of an MHW are described in Section 2.6). Blue dots are outliers, defined as months with F_{CO_2} 1.5 times higher than the distance between upper and lower quartiles (Matlab function *boxchart*).

atmospheric forcing, particularly through anomalous air-sea heat fluxes (Oliver et al., 2021), as seen with Blob 1.0 in SCCS (Zaba & Rudnick, 2016).

3.3.6. Impact of Marine Heatwaves in the Upwelling Regime

At CCE2, Blob 1.0 lasted 151 days, exceeding the average MHWs duration at this site (21 days). Unlike the open-ocean station, the $\delta pCO_{2,sw}$ was observed to be negative (on average −16 µatm) during Blob 1.0 (Figures 4b and 5h), and controlled by $pCO_{2,sw}^{\text{non-thermal}}$ processes. $\delta pCO_{2,sw}^{\text{non-thermal}}$, on average, contributed to a $pCO_{2,sw}$ decrease of −44 µatm while $\delta pCO_{2,sw}^{\text{thermal}}$ (SST) contribution was +28 µatm. The negative $\delta pCO_{2,sw}$ resulted in a negative $\delta\Delta pCO_2$ and a mean CO_2 uptake of −0.81 molC m^{-2} year^{-1} during Blob 1.0. The total F_{CO_2} over this event was −0.63 molC m^{-2}, a net uptake higher than the typical amount of CO_2 outgassed at this site annually.

In general, the $pCO_{2,sw}^{\text{non-thermal}}$ is influenced by various processes, including CO_2 consumption by phytoplankton, changes in TA due to calcification and nitrate utilization, air-sea CO_2 exchange, and variations in DIC and TA due to vertical and horizontal advection of different water masses (Takahashi et al., 2002). In this case, the low DIC was not due to anomalies in biology, as low surface Chl-a persisted throughout the event (Figures 5g and 5h), which would lead to positive (rather than negative) δDIC. The low Chl-a was attributed to the strong warming-related stratification in the upper 50 m, limiting nutrient input into the euphotic zone (Kahru et al., 2018; Lilly et al., 2019; Zaba & Rudnick, 2016). Furthermore, air-sea gas exchange cannot account for the anomalously low DIC since CO_2 uptake during Blob 1.0 was lower than the climatology (Figure 4). In the absence of pronounced TA changes, changes in advective processes are the only remaining cause of low DIC.

The negative $\delta pCO_{2,sw}$ could be attributed to a significant reduction in upwelling during Blob 1.0. We evaluated the upwelling conditions at CCE2 using an index developed for the U.S. West Coast: the Coastal Upwelling Transport Index (CUTI; Jacox et al., 2018). This index shows weak, year-round persistent upwelling at 34°N (Jorgensen et al., 2024), with stronger upwelling between February and July, transitioning to weak upwelling the rest of the year. During Blob 1.0, CUTI indicated little to no upwelling at 34°N (Figure S10 in Supporting Information S1). Reduced and less favorable wind stress (Figure 4h) adds to the suppressed upwelling hypothesis (Figure S8h in Supporting Information S1), likely accounting for the observed negative $\delta pCO_{2,sw}$, and δnDIC. Our findings illustrate that non-thermal processes, or in this case, their absence, play a pivotal role in offsetting the expected thermally-driven CO_2 outgassing during MHWs. This is particularly important because MHWs can help mitigate (temporarily) the CO_2 uptake, which contributes to ocean acidification in the ocean (Edwing et al., 2024; Mignot et al., 2022; Mogen et al., 2022).

At this site, only 10 months with MHWs (6% of the observations) were detected (red dots in Figure 6). These MHW months occurred between September and March, mainly during the weak upwelling season. The CCE2 site

Table 2
Trends and 95% Confidence Interval in Atmospheric and Seawater Surface pCO_2 and Its Components ($pCO_{2,sw}^{thermal}$ and $pCO_{2,sw}^{non\text{-}thermal}$), Together With the Corresponding Environmental Variables at the CCE Moorings for 2008–2022 at CCE1 and 2010–2022 at CCE2

	CCE1 mooring (2008–2022)	CCE2 mooring (2010–2022)
$pCO_{2,sw}$ (µatm year^{-1})	2.9 ± 0.3	2.1 ± 0.8
$pCO_{2,air}$ (µatm year^{-1})	2.3 ± 0.1	2.4 ± 0.1
$pCO_{2,sw}^{thermal}$ (µatm year^{-1})	0.9 ± 0.4	0.8 ± 0.5
$pCO_{2,sw}^{non\text{-}thermal}$ (µatm year^{-1})	2.1 ± 0.4	1.5 ± 1.2
SST (°C year^{-1})	0.06 ± 0.02	0.05 ± 0.03
SSS (year^{-1})	N.S.	0.011 ± 0.003
Wind Speed (m s^{-1} year^{-1})	N.S.	−0.03 ± 0.02
nDIC (µmol kg^{-1} year^{-1})	0.91 ± 0.29	1.17 ± 0.43
nTA (µmol kg^{-1} year^{-1})	N.S.	0.09 ± 0.05
DIC (µmol kg^{-1} year^{-1})	0.96 ± 0.29	1.79 ± 0.49

Note. The trends were estimated using the anomalies time series in Figures 3 and 4, and uncertainties were computed following Glover et al. (2011) and Sutton et al. (2022). Trends not significant are reported as N.S.

saw a small increase in CO_2 uptake in winter months affected by MHWs (November to March; Figure 6b). The observed CO_2 uptake was caused by unusually low $pCO_{2,sw}$ (and ΔpCO_2). As with Blob 1.0, there was no upwelling during these months, as revealed by the minimum values in the BEUTI and CUTI indexes. Low Chl-a and nDIC concentrations observed at the surface further confirm the similarities with Blob 1.0. All these factors contributed to $pCO_{2,sw}^{non\text{-}thermal}$, which outweighed the temperature effect. However, when MHWs occurred in September and October, we observed a small reversal of the climatological mean, with CO_2 outgassing. Here, warming and increased stratification of the water column resulted in increasing $pCO_{2,sw}$ and ΔpCO_2, with $pCO_{2,sw}^{thermal}$ dominating over non-thermal processes.

3.4. Trends in pCO_2 and CO_2 Fluxes

At the CCE moorings, de-seasonalized $pCO_{2,sw}$ and $pCO_{2,air}$ significantly increased between 2008 and 2022 (Table 2). The rate of increase in $pCO_{2,air}$ is similar at both sites while $pCO_{2,sw}$ has been increasing slightly faster in the open-ocean (2.9 µatm year^{-1}) than in the upwelling regime (2.2 µatm year^{-1}). Our estimated offshore $pCO_{2,sw}$ increase between 2008 and 2022 is approximately twice the rate of increase in $pCO_{2,sw}$ calculated at station 90.90 of CalCOFI between 1984 and 2021 by Wolfe et al. (2023) in a similar environment as CCE1. Our time series are more recent and shorter, and therefore, they capture a different part of the CO_2 curve compared with Wolfe et al. (2023). As a result, the more recent tangent to the CO_2 curve would have a greater slope compared with almost 40 years of measurements reported by Wolfe et al. (2023). The long-term trends in $pCO_{2,sw}$ at the CCE sites align with the expected behavior of seawater in equilibrium with rising atmospheric CO_2 concentrations, which is likely driving the changes offshore but not necessarily in the upwelling regime.

The non-thermal component ($pCO_{2,sw}^{non\text{-}thermal}$) is the primary driver of the increase in surface $pCO_{2,sw}$ at both sites, with a trend that is at least twice that of $pCO_{2,sw}^{thermal}$ (Table 2). Assuming that carbon internal sources and sinks do not change over time, the air-sea F_{CO_2} must remain the same to maintain this balance. The simplest way to achieve this is if the $pCO_{2,sw}$ follows the $pCO_{2,air}$ trend of 2.3–2.4 µmol year^{-1}, such that the mean difference (ΔpCO_2) remains the same. Our analysis shows that at CCE1, approximately 30% of the $pCO_{2,sw}$ trend comes from just the warming ($pCO_{2,sw}^{thermal}$; Table 2). This means that the air-sea fluxes need to increase the DIC to account for the remaining 70% of the required pCO_2 increase. This implies a DIC increase of 0.82 µmol kg^{-1} year^{-1} while we observe 0.96 µmol kg^{-1} year^{-1}, well within the uncertainty. Thus, the observed DIC increase probably results from adjustment to keep the ΔpCO_2 constant. Therefore, much of the difference in nDIC (and DIC) anomalies between the two La Niña events (2010/2011 and 2022) can be attributed to the increase in $pCO_{2,air}$. This is consistent with Wolfe et al. (2023), who showed that on a decadal timescale, the increase of total carbon was the major driver of $pCO_{2,sw}$, with a contribution of 93% at an open-ocean station located ∼127 km SW from CCE1.

Similarly, in the North Atlantic, McKinley et al. (2011) showed that $pCO_{2,sw}^{non\text{-}thermal}$ trends explained the observed oceanic pCO_2 trends, consistent with a long-term oceanic equilibrium with the atmospheric pCO_2.

At CCE2, it is more complicated due to a significant positive salinity and TA trend (Table 2). In a closed system, the TA trend alone would create a pCO_2 trend of approximately 0.16 µatm year^{-1}. The warming trend would make pCO_2 increase by 0.8 µatm year^{-1} (Table 2). Then, the DIC trend needed to keep the mean equilibrium with the $pCO_{2,air}$ is 1.2 µmol kg^{-1} year^{-1}. The observed change is somewhat larger but close to the uncertainty limits. The increase in salinity can lead to DIC changes, either by changing the concentration of the DIC ions or by small water-mass composition changes (the DIC-S relation for the local water mass suggests this; Bograd et al., 2019). Ren and Rudnick (2021) also reported a long-term increase in salinity since the 2000s, which is consistent with our observations at CCE2. Thus, the air-sea F_{CO_2} would not need to be implicated to create the new equilibrium and the required DIC changes at CCE2.

4. Conclusion

In this study, we used daily-averaged observations of pCO_2 collected by two moorings (CCE1 and CCE2) between 2008 and 2022 to estimate air-sea F_{CO_2} and constituents of the carbonate system. The two moorings are located in distinct oceanographic environments in the Southern California Current System: the open ocean (CCE1), and coastal seasonal upwelling (CCE2) regimes. We described, assessed, and contrasted the drivers of the $pCO_{2,sw}$ and air-sea F_{CO_2} in these regions.

Based on mean annual cycles derived from the long high-resolution time series, we demonstrate that within subtropical latitudes, distinct oceanographic regimes (open-ocean vs. upwelling) imply different drivers of $pCO_{2,sw}$ on an annual timescale. $pCO_{2,sw}$ and air-sea F_{CO_2} follows the annual cycle of SST at the open-ocean site while the upwelling of CO_2-rich waters at the surface controls $pCO_{2,sw}$, F_{CO_2}, and nDIC at the coastal site. Nearshore, the DIC cycle follows a DIC-water mass relationship modulated by local biological processes and air-sea F_{CO_2}. The net annual F_{CO_2} shows that the offshore region acts as a CO_2 sink from the atmosphere while the nearshore region is a CO_2 source to the atmosphere. On interannual timescales, the time-series anomalies of $pCO_{2,sw}$ and air-sea F_{CO_2} show extended periods of very low and high anomalies linked to strong ENSO events and MHWs. These events can intensify the F_{CO_2} magnitude or reverse the net fluxes at each site from a CO_2 sink to a source or vice versa. Air-sea F_{CO_2} and $pCO_{2,sw}$ anomalies are typically opposite at the two mooring locations during such events.

During MHWs, and particularly during Blob 1.0, the development of warm anomalies reached sub-surface depths and resulted in a deepening of the thermocline, thus inhibiting upwelling waters from reaching the surface at CCE2. We identified distinct drivers of associated carbon-system anomalies at the two sites during MHWs: (a) the absence of upwelling caused abnormally low $pCO_{2,sw}$ anomalies at the nearshore site resulting in anomalous CO_2 uptake; (b) increased SST at the offshore site resulted in an abnormal increase of $pCO_{2,sw}$, turning this site into a CO_2 source during MHWs. This result is particularly relevant nearshore, where we observe that non-thermal processes can counteract or mitigate the expected decrease in CO_2 uptake due to the rise of SST during MHWs.

Long-term trends of $pCO_{2,sw}$ were broadly consistent with the atmospheric pCO_2 trend. At the offshore regime, we found the $pCO_{2,sw}$ trend to be driven by air-sea F_{CO_2} that equilibrate air and sea pCO_2. On the other hand, in the upwelling site, the presence of a salinity trend implies that the required DIC trend for atmospheric equilibrium can also result from changing water-mass compositions or concentration due to freshwater loss.

Data Availability Statement

The pCO_2 data used in this paper (from both CCE moorings) are available at Sutton et al. (2019). OISST data can be found at Huang et al. (2021) and CCMP wind data are available at Mears et al. (2022). Temperature and salinity data from the CCE moorings in the upper 100 m is available at https://www.ncei.noaa.gov/thredds-ocean/catalog/ndbc/oceansites/DATA/CCE1/catalog.html (CCE1) and https://www.ncei.noaa.gov/thredds-ocean/catalog/ndbc/oceansites/DATA/CCE2/catalog.html (CCE2). Satellite-derived Chlorophyll data in the California Current System is available at https://spg-satdata.ucsd.edu/CC4km/ (Kahru et al., 2015, 2018). CalCOFI data are

available at https://calcofi.org, and water samples collected during cruises of mooring recovery and deployment are available at Send et al. (2016, 2022).

Acknowledgments
This study was supported by NOAA's Ocean Acidification Program (OAP, https://ror.org/02bfn4816) and Global Ocean Monitoring and Observing (GOMO, https://ror.org/037bamf06) Program under awards NA20OAR4320278, NA15OAR4320071, NA10OAR4320156, NA17RJ1231, and OAP1517-1027 and by NSF via the California Current Ecosystem Long-Term Ecological Research site. Carbon observations are supported by the Office of Oceanic and Atmospheric Research of NOAA, U.S. Department of Commerce, including resources from the Global Ocean Monitoring and Observing Program and the Ocean Acidification Program (Open Funder Registry numbers 100018302 and 100018228, respectively). We thank Mati Kahru for making the satellite Chl-a time series available, and Terence O'Brien for the discussion of the results. Additionally, we thank the numerous people, including commanding officers and captains from the NOAA and UNOLS ships, marine technicians, and the team of engineers and technicians from the SIO Ocean Time-Series Group and NOAA PMEL that have built and maintained the buoys and moorings over the past 16 years. This is PMEL contribution 5701.

References

Alin, S. R., Feely, R. A., Dickson, A. G., Hernández-Ayón, J. M., Juranek, L. W., Ohman, M. D., & Goericke, R. (2012). Robust empirical relationships for estimating the carbonate system in the Southern California Current System and application to CalCOFI hydrographic cruise data (2005—2011). *Journal of Geophysical Research*, *117*(C5), C05033. https://doi.org/10.1029/2011JC007511

Ayers, J. M., & Lozier, M. S. (2012). Unraveling dynamical controls on the North Pacific carbon sink. *Journal of Geophysical Research*, *118*(C1), C01017. https://doi.org/10.1029/2011JC007368

Bograd, S. J., Checkley, D. A., Jr., & Wooster, W. S. (2003). CalCOFI: A half century of physical, chemical, and biological research in the California Current System. *Deep Sea Research II: Topical Studies in Oceanography*, *50*(14–16), 2349–2353. https://doi.org/10.1016/S0967-0645(03)00122-X

Bograd, S. J., Schroeder, I., Sarkar, N., Qiu, X., Sydeman, W. J., & Schwing, F. B. (2009). Phenology of coastal upwelling in the California Current. *Geophysical Research Letters*, *36*(1), L01602. https://doi.org/10.1029/2008GL035933

Bograd, S. J., Schroeder, I. D., & Jacox, M. G. (2019). A water mass history of the Southern California Current System. *Geophysical Research Letters*, *46*(12), 6690–6698. https://doi.org/10.1029/2019GL082685

Borges, A. V., Delille, B., & Frankignoulle, M. (2005). Budgeting sinks and sources of CO_2 in the coastal ocean: Diversity of ecosystems counts. *Geophysical Research Letters*, *32*(14), L14601. https://doi.org/10.1029/2005GL023053

Brady, R. X., Lovenduski, N. S., Alexander, M. A., Jacox, M., & Gruber, N. (2019). On the role of climate modes in modulating the air-sea CO_2 fluxes in eastern boundary upwelling systems. *Biogeosciences*, *16*(2), 329–346. https://doi.org/10.5194/bg-16-329-2019

Cai, W.-J. (2011). Estuarine and coastal ocean carbon paradox: CO_2 sinks or sites of terrestrial carbon incineration? *Annual Reviews of Marine Science*, *3*(1), 123–145. https://doi.org/10.1146/annurev-marine-120709-142723

Cai, W.-J., Dai, M., & Wang, Y. (2006). Air-sea exchange of carbon dioxide in ocean margins: A province-based synthesis. *Geophysical Research Letters*, *33*(12), L12603. https://doi.org/10.1029/2006GL026219

Cai, W.-J., Hu, X., Huang, W.-J., Jiang, L.-Q., Wang, Y., Peng, T.-H., & Zhang, X. (2010). Alkalinity distribution in the western North Atlantic Ocean margins. *Journal of Geophysical Research*, *115*(C8), C08014. https://doi.org/10.1029/2009JC005482

Capotondi, A., Wittenberg, A., Newman, M., Di Lorenzo, E., Yu, J., Braconnot, P., et al. (2015). Understanding ENSO diversity. *Bulletin of the American Meteorological Society*, *96*(6), 921–938. https://doi.org/10.1175/BAMS-D-13-00117.1

Chen, S., & Hu, C. (2019). Environmental controls of surface water pCO_2 in different coastal environments: Observations from marine buoys. *Continental Shelf Research*, *183*, 73–86. https://doi.org/10.1016/j.csr.2019.06.007

Chen, S., Hu, C., Byrne, R. H., Robbins, L. L., & Yang, B. (2016). Remote estimation of surface pCO_2 on the West Florida shelf. *Continental Shelf Research*, *128*, 10–25. https://doi.org/10.1016/j.csr.2016.09.004

Chen, S., Sutton, A. J., Hu, C., & Chai, F. (2021). Quantifying the atmospheric CO_2 forcing effect on surface ocean pCO_2 in the North Pacific subtropical gyre in the past two decades. *Frontiers in Marine Science*, *8*, 636881. https://doi.org/10.3389/fmars.2021.636881

Chenillat, F., Rivière, P., Capet, X., Di Lorenzo, E., & Blanke, B. (2012). North Pacific Gyre Oscillation modulates seasonal timing and ecosystem functioning in the California Current upwelling system. *Geophysical Research Letters*, *39*(1), L01606. https://doi.org/10.1029/2011GL049966

Chhak, K., & Di Lorenzo, E. (2007). Decadal variations in the California Current upwelling cells. *Geophysical Research Letters*, *314*(14), L14604. https://doi.org/10.1029/2007GL030203

Crawford, W. J., Moore, A. M., Jacox, M. G., Fiechter, J., Neveu, E., & Edwards, C. A. (2018). A resonant response of the California Current circulation to forcing by low frequency climate variability. *Deep Sea Research II*, *151*, 16–36. https://doi.org/10.1016/j.dsr2.2017.07.016

Dalsin, M., Walter, R. K., & Mazzini, P. K. F. (2023). Effects of basin-scale climate modes and upwelling on nearshore marine heatwaves and cold spells in the California Current. *Scientific Reports*, *13*(1), 12389. https://doi.org/10.1038/s41598-023-39193-4

DeGrandpre, M. D., Olbu, G. J., Beatty, C. M., & Hammar, T. R. (2002). Air-sea CO_2 fluxes on the US Middle Atlantic Bight. *Deep-Sea Research II*, *49*(20), 4355–4367. https://doi.org/10.1016/S0967-0645(02)00122-4

Dickson, A. G. (1990a). Standard potential of the reaction: $AgCl(s) + 12H_2(g) = Ag(s) + HCl$ (aq), and the standard acidity constant of the ion HSO_4^- in synthetic sea water from 273.15 to 318.15 K. *Journal of Chemical Thermodynamics*, *22*(2), 113–127. https://doi.org/10.1016/0021-9614(90)90074-Z

Dickson, A. G. (1990b). Thermodynamics of the dissociation of boric acid in synthetic seawater from 273.15 to 318.15 K. *Deep-Sea Research Part A*, *37*(5), 755–766. https://doi.org/10.1016/0198-0149(90)90004-F

Dickson, A. G., & Millero, F. J. (1987). A comparison of the equilibrium constants for the dissociation of carbonic acid in seawater media. *Deep Sea Research Part A*, *34*(10), 1733–1743. https://doi.org/10.1016/0198-0149(87)90021-5

Di Lorenzo, E., Schneider, N., Cobb, K. M., Chhak, K., Franks, P. J. S., Miller, A. J., et al. (2008). North Pacific Gyre Oscillation links ocean climate and ecosystem change. *Geophysical Research Letters*, *35*(8), L08607. https://doi.org/10.1029/2007GL032838

Dore, J. E., Lukas, R., Sadler, D. W., & Karl, D. M. (2003). Climate-driven changes to the atmospheric CO_2 sink in the subtropical North Pacific Ocean. *Nature*, *424*(6950), 754–757. https://doi.org/10.1038/nature01885

Duke, P. J., Hamme, R. C., Ianson, D., Landschützer, P., Ahmed, M. M. M., Swart, N. C., & Covert, P. A. (2023). Estimating marine carbon uptake in the northeast Pacific using a neural network approach. *Biogeosciences*, *20*(18), 3919–3941. https://doi.org/10.5194/bg-20-3919-2023

Edwing, K., Wu, Z., Lu, W., Li, X., Cai, W.-J., & Yan, X.-H. (2024). Impact of marine heatwaves on air-sea CO_2 flux along the US East Coast. *Geophysical Research Letters*, *51*(1), e2023GL105363. https://doi.org/10.1029/2023GL105363

Fay, A. R., Gregor, L., Landschützer, P., McKinley, G. A., Gruber, N., Gehlen, M., et al. (2021). SeaFlux: Harmonization of air–sea CO_2 fluxes from surface pCO_2 data products using a standardized approach. *Earth System Science Data*, *13*(10), 4693–4710. https://doi.org/10.5194/essd-13-4693-2021

Fiechter, J., Curchitser, E. N., Edwards, C. A., Chai, F., Goebel, N. L., & Chavez, F. P. (2014). Air-sea CO_2 fluxes in the California Current: Impacts of model resolution and coastal topography. *Global Biogeochemical Cycles*, *28*(4), 371–385. https://doi.org/10.1002/2013GB004683

Franco, A. C., Ianson, D., Ross, T., Hamme, R. C., Monahan, A. H., Christian, J. R., et al. (2021). Anthropogenic and climatic contributions to observed carbon system trends in the northeast Pacific. *Global Biogeochemical Cycles*, *35*(7), e2020GB006829. https://doi.org/10.1029/2020GB006829

Friederich, G. E., Brewer, P. G., Herlien, R., & Chavez, F. P. (1995). Measurement of sea surface partial pressure of CO_2 from a moored buoy. *Deep-Sea Research Part I*, *42*(7), 1175–1186. https://doi.org/10.1016/0967-0637(95)00044-7

Friederich, G. E., Walz, P. M., Burczynski, M. G., & Chavez, F. P. (2002). Inorganic carbon in the central California upwelling system during the 1997–1999 El Niño-La Niña event. *Progress in Oceanography*, *54*(1–4), 185–203. https://doi.org/10.1016/S0079-6611(02)00049-6

Friedlingstein, P., O'Sullivan, M., Jones, M. W., Andrew, R. M., Bakker, D. C. E., Hauck, J., et al. (2023). Global carbon budget 2023. *Earth System Science Data*, *15*(12), 5301–5369. https://doi.org/10.5194/essd-15-5301-2023

Fumo, J. T., Carter, M. L., Flick, R. E., Rasmussen, L. L., Rudnick, D. L., & Iacobellis, S. F. (2020). Contextualizing marine heatwaves in the Southern California bight under anthropogenic climate change. *Journal of Geophysical Research: Oceans*, *125*(5), e2019JC015674. https://doi.org/10.1029/2019JC015674

Glover, D. M., Jenkins, W. J., & Doney, S. C. (2011). *Modeling methods for marine science*. Cambridge University Press.

Gray, S. E. C., DeGrandpre, M. D., Moore, T. S., Martz, T. R., Friederich, G. E., & Johnson, K. S. (2011). Applications of *in situ* pH measurements for inorganic carbon calculations. *Marine Chemistry*, *125*(1–4), 82–90. https://doi.org/10.1016/j.marchem.2011.02.005

Gregor, L., & Gruber, N. (2021). OceanSODA-ETHZ: A global gridded data set of the surface ocean carbonate system for seasonal to decadal studies of ocean acidification. *Earth System Science Data*, *13*(2), 777–808. https://doi.org/10.5194/essd-13-777-2021

Gruber, N. (2015). Carbon at the coastal interface. *Nature*, *517*(7533), 148–149. https://doi.org/10.1038/nature14082

Gruber, N., Bakker, D. C. E., DeVries, T., Gregor, L., Hauck, J., Landschützer, P., et al. (2023). Trends and variability in the ocean carbon sink. *Nature Reviews Earth and Environment*, *4*(2), 119–134. https://doi.org/10.1038/s43017-022-00381-x

Hales, B., Strutton, P. G., Saraceno, M., Letelier, R., Takahashi, T., Feely, R., et al. (2012). Satellite-based prediction of pCO_2 in coastal waters of the eastern North Pacific. *Progress in Oceanography*, *103*, 1–15. https://doi.org/10.1016/j.pocean.2012.03.001

Hobday, A. J., Alexander, L. V., Perkins, S. E., Smale, D. A., Straub, S. C., Oliver, E. C. J., et al. (2016). A hierarchical approach to defining marine heatwaves. *Progress in Oceanography*, *141*, 227–238. https://doi.org/10.1016/j.pocean.2015.12.014

Huang, B., Liu, C., Banzon, V., Freeman, E., Graham, G., Hankins, B., et al. (2021). Improvements of the Daily Optimum Interpolation Sea Surface Temperature (DOISST) Version 2.1 [Dataset]. *Journal of Climate*, *34*(8), 2923–2939. https://doi.org/10.1175/JCLI-D-20-0166.1

Hunt, C. W., Salisbury, J. E., Vandemark, D., Aβmann, S., Fietzek, P., Melrose, C., et al. (2021). Variability of USA East Coast surface total alkalinity distributions revealed by automated instrument measurements. *Marine Chemistry*, *232*, 103960. https://doi.org/10.1016/j.marchem.2021.103960

Ishii, M., Feely, R. A., Rodgers, K. B., Park, G.-H., Wanninkhof, R., Sasano, D., et al. (2014). Air-sea CO_2 flux in the Pacific Ocean for the period 1990–2009. *Biogeosciences*, *11*(3), 709–734. https://doi.org/10.5194/bg-11-709-2014

Jacox, M. G., Edwards, C. A., Hazen, E. L., & Bograd, S. J. (2018). Coastal upwelling revisited: Ekman, Bakun, and improved upwelling indices for the U.S. west coast. *Journal of Geophysical Research*, *123*(10), 7332–7350. https://doi.org/10.1029/2018JC014187

Jacox, M. G., Fiechter, J., Moore, A. M., & Edwards, C. A. (2015). ENSO and the California Current coastal upwelling response. *Journal of Geophysical Research: Oceans*, *120*(3), 1691–1702. https://doi.org/10.1002/2014JC010650

Jiang, Z.-P., Tyrrell, T., Hydes, D. J., Dai, M., & Hartman, S. E. (2014). Variability of alkalinity and the alkalinity-salinity relationship in the tropical and subtropical surface ocean. *Global Biogeochemical Cycles*, *28*(7), 729–742. https://doi.org/10.1002/2013GB004678

Jorgensen, E. M., Hazen, E. L., Jacox, M. G., Buil, M. P., Schroeder, I., & Bograd, S. J. (2024). Physical and biogeochemical phenology of coastal upwelling in the California Current System. *Geophysical Research Letters*, *51*(7), e2024GL108194. https://doi.org/10.1029/2024GL108194

Kahru, M., Jacox, M. G., & Ohman, M. D. (2018). CCE1: Decrease in the frequency of oceanic fronts and surface chlorophyll concentration in the California Current System during the 2014–2016 northeast Pacific warm anomalies. *Deep-Sea Research Part I*, *140*, 4–13. https://doi.org/10.1016/j.dsr.2018.04.007

Kahru, M., Kudela, R. M., Anderson, C. R., & Mitchell, B. G. (2015). Optimized merger of ocean color algorithms. *IEEE Geoscience and Remote Sensing Letters*, *12*(11), 2282–2285. https://doi.org/10.1109/LGRS.2015.2470250

Kahru, M., Kudela, R. M., Manzano-Sarabia, M., & Mitchell, B. G. (2012). Trends in the surface chlorophyll of the California Current: Merging data from multiple ocean color satellites. *Deep Sea Research Part II*, *77–80*, 89–98. https://doi.org/10.1016/j.dsr2.2012.04.007

Kohlman, C., Cronin, M. F., Dziak, R., Mellinger, D. K., Sutton, A., Galbraith, M., et al. (2024). The 2019 marine heatwave at Ocean Station Papa: A multi-disciplinary assessment of ocean conditions and impacts on marine ecosystems. *Journal of Geophysical Research: Oceans*, *129*(6), e2023JC020167. https://doi.org/10.1029/2023JC020167

Kosro, P. M., Huyer, A., Ramp, S. R., Smith, R. L., Chavez, F. P., Cowles, T. J., et al. (1991). The structure of the transition zone between coastal waters and the open ocean off northern California, winter and spring 1987. *Journal of Geophysical Research*, *96*(C8), 14707–14730. https://doi.org/10.1029/91JC01210

Landschützer, P., Gruber, N., & Bakker, D. C. E. (2016). Decadal variations and trends of the global ocean carbon sink. *Global Biogeochemical Cycles*, *30*(10), 1396–1417. https://doi.org/10.1002/2015GB005359

Landschützer, P., Ilyina, T., & Lovenduski, N. S. (2019). Detecting regional modes of variability in observation-based surface ocean pCO_2. *Geophysical Research Letters*, *46*(5), 2670–2679. https://doi.org/10.1029/2018GL081756

Laruelle, G. G., Dürr, H. H., Slomp, C. P., & Borges, A. V. (2010). Evaluation of sinks and sources of CO_2 in the global coastal ocean using a spatially-explicit typology of estuaries and continental shelves. *Geophysical Research Letters*, *47*, L15607. https://doi.org/10.1029/2010GL043691

Laruelle, G. G., Landschützer, P., Gruber, N., Tison, J.-L., Delille, B., & Regnier, P. (2017). Global high-resolution monthly pCO_2 climatology for the coastal ocean derived from neural network interpolation. *Biogeosciences*, *14*(19), 4545–4561. https://doi.org/10.5194/bg-14-4545-2017

Laruelle, G. G., Lauerwald, R., Pfeil, B., & Regnier, P. (2014). Regionalized global budget of the CO_2 exchange at the air-water interface in continental shelf seas. *Global Biogeochemical Cycles*, *28*(11), 1199–1214. https://doi.org/10.1002/2014GB004832

Lee, K., Tong, L. T., Millero, F. J., Sabine, C. L., Dickson, A. G., Goyet, C., et al. (2006). Global relationships of total alkalinity with salinity and temperature in surface waters of the world's oceans. *Geophysical Research Letters*, *33*(19), L19605. https://doi.org/10.1029/2006GL027207

Leinweber, A., Gruber, N., Frenzel, H., Friederich, G. E., & Chavez, F. P. (2009). Diurnal carbon cycling in the surface ocean and lower atmosphere of Santa Monica Bay, California. *Geophysical Research Letters*, *36*(8), L08601. https://doi.org/10.1029/2008GL037018

Le Quéré, C., Andrew, R. M., Canadell, J. G., Sitch, S., Korsbakken, J. I., Peters, G. P., et al. (2016). Global carbon budget 2016. *Earth System Science Data*, *8*(2), 605–649. https://doi.org/10.5194/essd-8-605-2016

Lewis, E., & Wallace, D. W. R. (1998). *Program developed for CO_2 system calculations*. ORNL/CDIAC-105 (p. 38). Carbon Dioxide Information Analysis Center, Oak Ridge National Laboratory. Retrieved from https://salish-sea.pnnl.gov/media/ORNL-CDIAC-105.pdf

Lilly, L. E., Send, U., Lankhorst, M., Martz, T. R., Feely, R. A., Sutton, A. J., & Ohman, M. D. (2019). Biogeochemical anomalies at two Southern California Current System moorings during the 2014–2016 warm anomaly-El Nino sequence. *Journal of Geophysical Research: Oceans*, *124*(10), 6886–6903. https://doi.org/10.1029/2019JC015255

Lowcher, C. F. (2023). *Upwelling and circulation dynamics in the Southern California Current System*. UC San Diego. Retrieved from https://escholarship.org/uc/item/41f2q923

Lynn, R. D., & Simpson, J. J. (1987). The California Current system: The seasonal variability of its physical characteristics. *Journal of Geophysical Research*, *92*(C12), 12947–12966. https://doi.org/10.1029/JC092iC12p12947

Mantua, N. J., & Hare, S. R. (2002). The Pacific decadal oscillation. *Journal of Oceanography*, *58*(1), 35–44. https://doi.org/10.1023/a:1015820616384

McClatchie, S., Goericke, R., Leising, A., Auth, T., Bjorkstedt, E., Robertson, R., et al. (2016). *State of the California Current 2015–16: Comparisons with the 1997–98 El Nino*. UC Santa Cruz. Retrieved from https://escholarship.org/uc/item/730558jh

McKinley, G. A., Fay, A. R., Takahashi, T., & Metzl, N. (2011). Convergence of atmospheric and North Atlantic carbon dioxide trends on multidecadal timescales. *Nature Geoscience*, *4*(9), 606–610. https://doi.org/10.1038/ngeo1193

Mears, C., Lee, T., Ricciardulli, L., Wang, X., & Wentz, F. (2022). RSS Cross-Calibrated Multi-Platform (CCMP) 6-hourly ocean vector wind analysis on 0.25 deg grid, Version 3.0 [Dataset]. *Remote Sensing Systems*. https://doi.org/10.56236/RSS-uv6h30

Mehrbach, C., Culberson, C. H., Hawley, J. E., & Pytkowicx, R. M. (1973). Measurement of the apparent dissociated constants of carbonic acid in seawater at atmospheric pressure. *Limnology and Oceanography*, *18*(6), 897–907. https://doi.org/10.4319/lo.1973.18.6.0897

Mignot, A., von Schuckmann, K., Landschutzer, P., Gasparin, F., van Gennip, S., Perruche, C., et al. (2022). Decrease in air-sea CO_2 fluxes caused by persistent marine heatwaves. *Nature Communications*, *13*(1), 4300. https://doi.org/10.1038/s41467-022-31983-0

Millero, F. J., Lee, K., & Roche, M. (1998). Distribution of alkalinity in the surface waters of the major oceans. *Marine Chemistry*, *60*(1–2), 111–130. https://doi.org/10.1016/S0304-4203(97)00084-4

Mogen, S. C., Lovenduski, N. S., Dallmann, A. R., Gregor, L., Sutton, A. J., Bograd, S. J., et al. (2022). Ocean biogeochemical signatures of the North Pacific Blob. *Geophysical Research Letters*, *49*(9), e2021GL096938. https://doi.org/10.1029/2021GL096938

Oliver, E. C. J., Benthuysen, J. A., Darmaraki, S., Donat, M. G., Hobday, A. J., Holbrook, N. J., et al. (2021). Marine heatwaves. *Annual Review of Marine Science*, *13*(1), 313–342. https://doi.org/10.1146/annurev-marine-032720-095144

Orr, J. C., Epitalon, J.-M., Dickson, A. G., & Gattuso, J.-P. (2018). Routine uncertainty propagation for the marine carbon dioxide system. *Marine Chemistry*, *207*, 84–107. https://doi.org/10.1016/j.marchem.2018.10.006

Palevsky, H. L., & Quay, P. D. (2017). Influence of biological carbon export on ocean carbon uptake over the annual cycle across the North Pacific Ocean. *Global Biogeochemical Cycles*, *31*(1), 81–95. https://doi.org/10.1002/2016GB005527

Pennington, J., Castro, C., Collins, C., Evans, W., Friederich, G., Michisaki, R., et al. (2010). The northern and central California coastal upwelling system. In K.-K. Liu, L. Atkinson, R. Quiñones, & L. Talaue-McManus (Eds.), *Carbon and nutrient fluxes in continental margins*, *Global Change The IGBP Series* (pp. 29–44). Springer Berlin Heidelberg.

Ren, A. S., & Rudnick, D. L. (2021). Temperature and salinity extremes from 2014–2019 in the California Current System and its source waters. *Communications Earth & Environment*, *2*(1), 62. https://doi.org/10.1038/s43247-021-00131-9

Rudnick, D. L., Zaba, K. D., Todd, R. E., & David, R. E. (2017). A climatology of the California Current System from a network of underwater gliders. *Progress in Oceanography*, *154*, 64–106. https://doi.org/10.1016/j.pocean.2017.03.002

Sabine, C. L., Feely, R. A., Gruber, N., Key, R. M., Lee, K., Bullister, J. L., et al. (2004). The oceanic sink for anthropogenic CO_2. *Science*, *305*(5682), 367–371. https://doi.org/10.1126/science.1097403

Send, U., Ohman, M., Lankhorst, M., & Kim, H.-J. (2016). Dissolved inorganic carbon, total alkalinity, nutrients, and other variables collected from profile and discrete observations using CTD, Niskin bottle, and other instruments from R/V New Horizon and R/V Robert Gordon Sproul in the U.S. West Coast for calibration and validation of California Current Ecosystem (CCE) Moorings from 2009-12-15 to 2015-04-29 (NCEI Accession 0146024) [Dataset]. *DATA.GOV*. https://doi.org/10.7289/v57d2s6c

Send, U., Ohman, M., Lankhorst, M., & Sevadjian, J. (2022). Dissolved inorganic carbon (DIC), total alkalinity (TA), temperature, salinity, nutrients, dissolved oxygen, chlorophyll-a and phaeo pigment measured by discrete water samples and CTD for calibration and validation of California Current Ecosystem (CCE) mooring timeseries from 2015-11-17 to 2021-06-18 (NCEI Accession 0249587) [Dataset]. *DATA.GOV*. https://doi.org/10.25921/35v7-2d22

Sharp, J. D., Fassbender, A. J., Carter, B. R., Lavin, P. D., & Sutton, A. J. (2022). A monthly surface pCO_2 product for the California Current Large Marine Ecosystem. *Earth System Science Data*, *14*(4), 2081–2108. https://doi.org/10.5194/essd-14-2081-2022

Song, R., DeVries, T., Li, R., Sutton, A. J., Send, U., & Frazão, H. C. (2025). High-frequency correlations between winds and pCO_2 change a coastal upwelling region from a CO_2 sink to a source. *Accepted in Geophysical Research Letters*.

Sutton, A. J., Battisti, R., Carter, B., Evans, W., Newton, J., Alin, S., et al. (2022). Advancing best practices for assessing trends of ocean acidification time series. *Frontiers in Marine Science*, *9*, 1045667. https://doi.org/10.3389/fmars.2022.1045667

Sutton, A. J., Feely, R. A., Maenner-Jones, S., Musielwicz, S., Osborne, J., Dietrich, C., et al. (2019). Autonomous seawater pCO_2 and pH time series from 40 surface buoys and the emergence of anthropogenic trends [Dataset]. *Earth System Science Data*, *11*(1), 421–430. https://doi.org/10.5194/essd-11-421-2019

Sutton, A. J., Sabine, C. L., Maenner-Jones, S., Lawrence-Slavas, N., Meinig, C., Feely, R. A., et al. (2014). A high-frequency atmospheric and seawater pCO_2 data set from 14 open-ocean sites using a moored autonomous system. *Earth System Science Data*, *6*(2), 353–366. https://doi.org/10.5194/essd-6-353-2014

Sutton, A. J., Wanninkhof, R., Sabine, C. L., Feely, R. A., Cronin, M. F., & Weller, R. A. (2017). Variability and trends in surface seawater pCO_2 and CO_2 flux in the Pacific Ocean. *Geophysical Research Letters*, *44*(11), 5627–5636. https://doi.org/10.1002/2017GL073814

Takahashi, T., Olafsson, K., Goddard, J. G., Chipman, D. W., & Sutherland, S. C. (1993). Seasonal variations of CO_2 and nutrients in the high-latitude surface oceans: A comparative study. *Global Biogeochemical Cycles*, *7*(4), 843–878. https://doi.org/10.1029/93gb02263

Takahashi, T., Sutherland, S. C., Sweeney, C., Poisson, A., Metzl, N., Tilbrook, B., et al. (2002). Global sea-air CO_2 flux based on climatological surface ocean pCO_2, and seasonal biological and temperature effects. *Deep-Sea Research II*, *49*(9–10), 1601–1622. https://doi.org/10.1016/S0967-0645(02)00003-6

Takahashi, T., Sutherland, S. C., Wanninkhof, R., Sweeney, C., Feely, R. A., Chipman, D. W., et al. (2009). Climatological mean and decadal change in surface ocean pCO_2, and net sea-air CO_2 flux over the global oceans. *Deep-Sea Research II*, *56*(8–10), 554–577. https://doi.org/10.1016/j.dsr2.2008.12.009

Tamburri, M. N., Johengen, T. H., Atkinson, M. J., Schar, D. W. H., Robertson, C. Y., Purcell, H., et al. (2011). Alliance for coastal technologies: Advancing moored pCO_2 instruments in coastal waters. *Marine Technology Society Journal*, *45*(1), 43–51. https://doi.org/10.4031/MTSJ.45.1.4

Thompson, A. R., Bjorkstedt, E. P., Bograd, S. J., Fisher, J. L., Hazen, E. L., Leising, A., et al. (2022). State of the California Current Ecosystem in 2021: Winter is coming? *Frontiers in Marine Science*, *9*, 958727. https://doi.org/10.3389/fmars.2022.958727

Todd, R. E., Rudnick, D. L., Davis, R. E., & Ohman, M. D. (2011). Underwater gliders reveal rapid arrival of El Niño effects off California's coast. *Geophysical Research Letters*, *38*(3), L03609. https://doi.org/10.1029/2010GL046376

Turi, G., Lachkar, Z., & Gruber, N. (2014). Spatiotemporal variability and drivers of pCO_2 and air–sea CO_2 fluxes in the California Current System: An eddy-resolving modeling study. *Biogeosciences*, *11*(3), 671–690. https://doi.org/10.5194/bg-11-671-2014

Uppstrom, L. R. (1974). The boron/chloronity ration of deep-sea water from the Pacific Ocean. *Deep-Sea Research*, *21*(2), 161–162. https://doi.org/10.1016/0011-7471(74)90074-6

Valsala, V., Maksyutov, S., Telszewski, M., Nakaoka, S., Nojiri, Y., Ikeda, M., & Murtugudde, R. (2012). Climate impacts on the structures of the North Pacific air-sea CO_2 flux variability. *Biogeosciences*, *9*(1), 477–492. https://doi.org/10.5194/bg-9-477-2012

Vandemark, D., Salisbury, J. E., Hunt, C. W., Shellito, S. M., Irish, J. D., McGillis, W. R., et al. (2011). Temporal and spatial dynamics of CO_2 air-sea flux in the Gulf of Maine. *Journal of Geophysical Research*, *116*(C1), C01012. https://doi.org/10.1029/2010JC006408

van Heuven, S., Pierrot, D., Rae, J. W. B., Lewis, E., & Wallace, D. W. R. (2011). MATLAB Program Developed for CO_2 system calculations ORNL/CDIAC-105b.[Software]. *Carbon Dioxide Information Analysis Center, Oak Ridge National Laboratory, U.S. Department of Energy*. https://doi.org/10.3334/CDIAC/otg.CO2SYS_MATLAB_v1.1

Wanninkhof, R. (2014). Relationship between wind speed and gas exchange over the ocean revisited. *Limnology and Oceanography: Methods*, *12*(6), 351–362. https://doi.org/10.4319/lom.2014.12.351

Wei, X., Li, K.-Y., Kilpatrick, T., Wang, M., & Xie, S.-P. (2021). Large-scale conditions for the record-setting Southern California marine heatwave of August 2018. *Geophysical Research Letters*, *48*(7), e2020GL091803. https://doi.org/10.1029/2020GL091803

Weiss, R. F. (1974). Carbon dioxide in water and seawater: The solubility of non-ideal gas. *Marine Chemistry*, *2*(3), 203–215. https://doi.org/10.1016/0304-4203(74)90015-2

Williams, N. L., Jurasek, L. W., Feely, R. A., Russell, J. L., Johnson, K. S., & Hales, B. (2018). Assessment of the carbonate chemistry seasonal cycles in the Southern Ocean from persistent observational platforms. *Journal of Geophysical Research: Oceans*, *123*(7), 4833–4852. https://doi.org/10.1029/2017JC012917

Wolfe, W. H., Martz, T. R., Dickson, A. G., Goericke, R., & Ohman, M. D. (2023). A 37-year record of ocean acidification in the Southern California current. *Communications Earth & Environment*, *4*(1), 406. https://doi.org/10.1038/s43247-023-01065-0

Xiu, P., & Chai, F. (2014). Variability of oceanic carbon cycle in the North Pacific from seasonal to decadal scales. *Journal of Geophysical Research: Oceans*, *119*(8), 5270–5288. https://doi.org/10.1002/2013JC009505

Zaba, K. D., & Rudnick, D. L. (2016). The 2014-2015 warming anomaly in the Southern California Current System observed by underwater gliders. *Geophysical Research Letters*, *43*(3), 1241–1248. https://doi.org/10.1002/2015GL067550

Zhang, Y., Wallace, J. M., & Battisti, D. S. (1997). ENSO-like interdecadal Variability: 1900–93. *Journal of Climate*, *10*(5), 1004–1020. https://doi.org/10.1175/1520-0442(1997)010<1004:ELIV>2.0.CO;2

References From the Supporting Information

Albuquerque, C., Miguel, G., de Oliveira Farias, C., Pinho, L., Marotta, H., Orselli, I. B. M., et al. (2025). Regional relationship between total alkalinity and salinity in the surface waters of the western South Atlantic margin. *Regional Studies in Marine Science*, *81*, 103992. https://doi.org/10.1016/j.rsma.2024.103992

Evans, W., Mathis, J. T., Ramsay, J., & Hetrick, J. (2015). On the frontline: Tracking ocean acidification in an Alaskan shellfish hatchery. *PLoS One*, *10*(7), e0130384. https://doi.org/10.1371/journal.pone.0130384

Gray, S. E. C., DeGrandpre, M. D., Moore, T. S., Martz, T. R., Friederich, G. E., & Johnson, K. S. (2011). Application of *in situ* pH measurements for inorganic carbon calculations. *Marine Chemistry*, *125*(1–4), 82–90. https://doi.org/10.1016/j.marchem.2011.02.005

Sutton, A. J., Sabine, C. L., Feely, R. A., Cai, W. J., Cronin, M. F., Mcphaden, M. J., et al. (2016). Using present-day observations to detect when anthropogenic change forces surface ocean carbonate chemistry outside preindustrial bounds. *Biogeosciences*, *13*(17), 5065–5083. https://doi.org/10.5194/bg-13-5065-2016